

Title: Mechanistic insight into RET kinase inhibitors targeting the DFG-out conformation in *RET*-rearranged cancer

Authors: D. Plenker^{1,2,§}, M. Riedel^{1,2,§}, J. Brägelmann^{1,2}, M. A. Dammert^{1,2}, R. Chauhan³, P. P. Knowles³, C. Lorenz^{1,2}, M. Keul⁷, M. Bührmann⁷, O. Pagel⁴, V. Tischler², A. H. Scheel⁵, D. Schütte², Y. Song⁶, J. Stark⁷, F. Mrugalla⁷, Y. Alber⁷, A. Richters⁷, J. Engel⁷, F. Leenders⁸, J. M. Heuckmann⁸, J. Wolf⁹, J. Diebold¹⁰, G. Pall¹¹, M. Peifer², M. Aerts^{12,13}, K. Gevaert^{12,13}, R. P. Zahedi⁴, R. Buettner⁵, K. M. Shokat¹⁴, N. Q. McDonald^{3,15}, S. M. Kast⁷, O. Gautschi^{10,†}, R. K. Thomas^{2,9,16,†} and M. L. Sos^{1,2,†,*}

Affiliations:

¹Molecular Pathology, Institute of Pathology, Center of Integrated Oncology, University Hospital Cologne, 50937, Cologne, Germany.

²Department of Translational Genomics, Center of Integrated Oncology Cologne–Bonn, Medical Faculty, University of Cologne, 50931, Cologne, Germany.

³Structural Biology Laboratory, Francis Crick Institute, 44 Lincoln's Inn Fields, London WC2A 3LY, UK

⁴Leibniz-Institut für Analytische Wissenschaften – ISAS – e.V., Dortmund, Germany

⁵Institute of Pathology, Center of Integrated Oncology, University Hospital Cologne, 50937, Cologne, Germany.

⁶Crown Bioscience, Inc. 3375 Scott Blvd, suite 108, Santa Clara, CA 95054, USA.

⁷Faculty of Chemistry and Chemical Biology, TU Dortmund University, 44227, Dortmund, Germany.

⁸NEO New Oncology GmbH, 51105, Cologne, Germany.

⁹Department of Internal Medicine, Center for Integrated Oncology Köln-Bonn,

University Hospital Cologne, Cologne, 50931, Cologne, Germany.

¹⁰Cancer Center, Lucerne Cantonal Hospital, 6000 Lucerne, Switzerland

¹¹Department of Internal Medicine 5, University Hospital Innsbruck, Hematology/Oncology, Anichstraße 35, 6020 Innsbruck, Austria

¹²VIB-UGent Center for Medical Biotechnology, VIB, B-9000 Ghent, Belgium

¹³Department of Biochemistry, Ghent University, B-9000 Ghent, Belgium

¹⁴Department of Cellular and Molecular Pharmacology, Howard Hughes Medical Institute, University of California, San Francisco, CA 94158, USA

¹⁵Institute of Structural and Molecular Biology, Department of Biological Sciences, Birkbeck College, Malet Street, London WC1E 7HX, UK

¹⁶German Cancer Consortium (DKTK), partner site Heidelberg and German Cancer Research Center (DKFZ), Heidelberg, Germany

* To whom correspondence should be addressed:

Martin L. Sos; martin.sos@uni-koeln.de

[§] These authors contributed equally to this work

[†] These authors contributed equally to this work

One Sentence Summary:

Our work provides mechanistic insights into the activity profiles of RET inhibitors that bind in the DFG-out conformation of RET and may be of importance for the effective treatment of *RET*-rearranged cancers.

Abstract

Oncogenic fusion events have been identified in a broad range of tumors. Among them, *RET* rearrangements represent distinct and potentially druggable targets that are recurrently found in lung adenocarcinomas. Here, we provide further evidence that current anti-RET drugs may not be potent enough to induce durable responses in such tumors. We report that potent inhibitors such as AD80 or ponatinib that stably bind in the DFG-out conformation of RET may overcome these limitations and selectively kill *RET*-rearranged tumors. Using chemical genomics in conjunction with phosphoproteomic analyses in *RET*-rearranged cells we identify the *CCDC6-RET*^{T788N} mutation and drug-induced MAPK pathway reactivation as possible mechanisms, by which tumors may escape the activity of RET inhibitors. Our data provide mechanistic insight into the druggability of RET kinase fusions that may be of help for the development of effective therapies targeting such tumors.

Introduction

Targeted inhibition of oncogenic driver mutations with small molecules represents the cornerstone of precision cancer medicine. *RET* rearrangements have been identified in a broad range of tumors including 1-2% of lung adenocarcinomas and their discovery sparked the hope for an effective treatment option in these patients (1-3). However, when compared to other oncogenic "driver" alterations such as rearranged ALK, rearranged RET seems to represent a difficult target as to date, no drug has been successfully established for the treatment of these tumors (4-6). Recent clinical data suggest that overall response rates in patients treated with currently available RET targeted drugs are rather limited and range between 18% - 53% (7-10). Improved selection of patients based on deep sequencing of individual tumors may help to

increase these response rates but still progression-free survival seems to be very limited (8-11). These observations are particularly surprising from a chemical point of view since a broad spectrum of kinase inhibitors is known to bind to RET and to inhibit its kinase activity *in vitro*.

Based on these observations we sought to characterize rearranged RET in orthogonal cancer models to identify potent RET inhibitors with high selectivity and optimal biochemical profile to target *RET*-rearranged tumors.

Results

Kinase inhibitor AD80 shows extraordinary activity in *RET*-rearranged cancer models

Since clinical experience with RET targeted drugs in lung cancer patients is rather disappointing we sought to test a series of clinically and preclinically available drugs with anti-RET activity in Ba/F3 cells engineered to express either *KIF5B-RET* or *CCDC6-RET* (1, 2, 12, 13). In these experiments, AD80 and ponatinib exhibited 100- to 1000-fold higher cytotoxicity compared to all other tested drugs in RET-dependent, but not IL-3 supplemented Ba/F3 cells (**Fig. 1A; Fig. S1A,B**). In line with these results, AD80, but not cabozantinib or vandetanib prevented phosphorylation of RET as well as of ERK, AKT and S6K at low nanomolar concentrations in *KIF5B-RET* expressing Ba/F3 cells (**Fig. 1B, Supplementary Table 1**).

To validate the efficacy of AD80 and ponatinib in an orthogonal model, we induced *KIF5B-RET* rearrangements (*KIF5B* exon 15; *RET* exon 12) in NIH-3T3 cells using CRISPR/Cas9-mediated genome editing. We confirmed their anchorage-independent growth, increased proliferation rate and their high sensitivity to AD80 and ponatinib (**Fig. 1C; Fig. S1C-E**) (14). Again, treatment with AD80 but not

cabozantinib or vandetanib led to inhibition of phospho-RET and of downstream effectors of RET signaling at low nanomolar concentrations (**Fig. 1D**). Interestingly, AD80 led to dephosphorylation of S6 also in parental NIH-3T3 cells and Ba/F3^{myr-AKT} control cells suggesting that S6 may represent an off-target at micromolar concentrations (**Fig. 1D; Fig. S1F**) (12).

To further substantiate our results, we next tested our panel of RET inhibitors in the *CCDC6-RET* rearranged lung adenocarcinoma cell line LC-2/AD (15). We observed similar activity profiles with AD80 followed by ponatinib as the most potent inhibitors compared to all other tested drugs in terms of cytotoxicity at low nanomolar concentrations (**Fig. 1E**) and inhibition of phospho-RET and other downstream signaling molecules (**Fig. 1F**).

Overall, our data suggest that in *RET*-rearranged cells AD80 and ponatinib are 100- to 1000-fold more effective against RET and its downstream signaling than any other clinically tested anti-RET drug.

Highly specific and effective inhibition of RET fusions in DFG-out conformation

To benchmark the genotype-specific activity of AD80 and ponatinib against well described kinase inhibitors such as erlotinib, BGJ398, vandetanib, cabozantinib, regorafenib, alectinib and ceritinib in a panel of 18 cancer cell lines driven by known oncogenic lesions such as mutant EGFR or rearranged ALK, including two *RET*-rearranged cells (LC-2/AD and TPC-1) (**Fig. S2A**) (6, 13, 16). Again, we identified AD80 and ponatinib as the most effective drug and through the calculation of median on-target vs. off-target ratios also as the most specific drugs in *RET*-fusion positive cells (**Fig. S2B; Supplementary Table 2**).

To further characterize intracellular signaling induced by a RET-inhibitor like AD80 we performed mass-spectrometry based phosphoproteomic analyses of LC-2/AD cells treated with 10nM or 100nM of AD80. In AD80 treated cells we observed a significant decrease of RET-Y900 phosphorylation with \log_2 -fold changes of -1.07 ($p=0.009$; 10nM AD80) and -2.11 ($p=0.0002$; 100nM AD80), respectively (**Fig. 2A**). Among all phospho-peptides quantified under control, 10nM and 100nM conditions ($n=11912$), the abundance of RET^{Y900} was among the most decreased phospho-peptides (ctrl. vs 100nM AD80; $p=0.00024$) and the most decreased receptor tyrosine kinases (**Fig. S2C**). These results highlight that in these cells RET is the primary target of AD80.

Based on these observations, we speculated that activation of RET-independent signaling pathways should largely abrogate the cytotoxic effects of AD80. To this end we supplemented LC-2/AD cells with exogenous receptor ligands and found that activity of AD80 was significantly reduced through addition of EGF, HGF and NRG1 indicating that RET is indeed the primary cellular target in *RET*-rearranged LC-2/AD cells (**Fig. S3A**).

To further characterize the high potency of AD80 and ponatinib against RET kinase fusions we expressed and purified different truncated versions of the RET core kinase and juxtamembrane-kinase domain as well as truncated forms of both CCDC6 (Δ CCDC6-KD) or KIF5B (Δ KIF5B-KD) kinase domain fusions (**Fig. S3B,C**) (17). We used these different RET-fusion kinase domain constructs to determine the extent to which binding of a given compound has an effect on protein thermal stability as measured by the melting temperature (T_m). The difference of melting temperature with and without drug (ΔT_m) extrapolates the potency of the individual drugs against the respective constructs (17). To our surprise, we found that treatment with the type I

inhibitors sunitinib or vandetanib resulted in a ΔT_m of only 1-4°C whereas the type II inhibitors sorafenib, ponatinib or AD80 increased the ΔT_m up to 10-18°C (**Fig. 2B; Fig. S3D-H**). We observed the strongest effects in $\Delta KIF5B$ -KD and $\Delta CCDC6$ -KD constructs treated with AD80 and core KD with ponatinib (**Fig. 2B; Fig. S3D; Supplementary Table 3**). Interestingly, this strong shift for inhibitors that stabilize the DFG-out conformation does not correlate with the differential *in vitro* kinase activity observed for sorafenib and other RET inhibitors (**Supplementary Table 4**) (6).

To further characterize the relevance of a DFG-out conformation for the activity of RET inhibitors we performed structural analyses. We employed homology modelling based on a VEGFR kinase (pdb code 2OH4 (18)) in the DFG-out complex, followed by extensive molecular dynamics (MD) simulation refinement, similar to a previously published methodology (19). We observed that the RMSD values remained largely stable over the time course of the MD simulation (RET-wt and RET-V804M) thus supporting our proposed model in which AD80 binds in the DFG-out conformation of the kinase (**Fig. S4A**). In this model AD80 forms an H-bond between the aspartate of the DFG motif that may be involved in the stabilization of the DFG-out conformation (**Fig. 3A**). A similar H-bond is also observed for cabozantinib, a known type II inhibitor, bound to RET-wt (**Fig. S4B**, see Supplementary Methods for model generation). This finding corroborates the validity of our binding mode hypothesis, though the pose is biased by construction, being based on the refined RET-wt/AD80 structure. Furthermore, we developed a binding pose model for AD57 (derivative of AD80) bound to RET-wt (see below) which, upon superimposition, displays considerable similarity with the experimentally determined structure of AD57 bound to cSrc (PDB code 3EL8) in the DFG-out form, again validating our approach (**Fig.**

S4C, Fig. S3H). Next we performed free energy MD simulations to transform AD80 into AD57. The calculations yield a binding free energy difference of $\Delta\Delta G^\circ = -0.21 \pm 0.17$ kcal mol⁻¹ at 25°C, which compares well with the values derived from IC₅₀ in *in vitro* kinase measurements. These latter concentration-based measures of binding affinity translate into an experimental estimate of the binding free energy difference of -0.41 kcal mol⁻¹ with IC₅₀(AD57) of 2nM and IC₅₀(AD80) of 4nM (see Supplementary methods) (12). Using as an alternative computational approach an integral equation approximation (see Supplementary Methods) we obtain 0.1 kcal mol⁻¹, also in close correspondence with both MD and experimental results. Thus, these analyses further support the proposed DFG-out conformation as the preferred binding mode since such agreement between experiment and theory would not have been expected if the true and predicted binding modes were largely dissimilar.

Overall, our cellular screening, phosphoproteomic, biochemical and structural data indicate that potent type II inhibitors like AD80 or ponatinib have an optimal RET specific profile that distinguishes them from currently available anti-RET drugs.

Differential activity of RET inhibitors against RET kinase gatekeeper mutation

Secondary resistance mutations frequently target a conserved residue, termed gatekeeper that controls access to a hydrophobic subpocket of the kinase domain (20). To test the impact of the gatekeeper resistance mutations on RET inhibitors we established Ba/F3 cells expressing *KIF5B-RET*^{V804M} or *CCDC6-RET*^{V804M} and tested them against a panel of different drugs. As expected only ponatinib but also AD80 showed high activity in these gatekeeper mutant cells (**Fig. 3B**) (21). Similar activity was observed when testing the AD80 derivatives AD57 and AD81 for their inhibitory potential on Ba/F3 cells expressing wild type and V804M mutated *KIF5B-RET* or

CCDC6-RET (**Fig. S5A**). This effect was also evident in the ability of AD80 to inhibit phosphorylation of RET as well as of ERK, AKT and S6K in these cells (**Fig. 3C, Supplementary Table S1**). Next, we used computational homology modeling coupled with MD refinement of AD80 in RET^{wt} in comparison with RET^{V804M}-mutant kinases. In line with our *in vitro* results, this analysis revealed high structural similarity and similar binding free energy estimates for both variants (-2.5 kcal mol⁻¹ for transforming RET^{wt} to RET^{V804M} bound to AD80 from the integral equation model) (**Fig. 3A, Supplementary Methods**).

In parallel, we noticed that independent of the individual treatment, RET phosphorylation levels tended to be higher in gatekeeper mutant cells when compared to wild type RET (**Fig. 3D**). To further characterize these differences we performed *in vitro* kinase assays and found that the introduction of the *RET*^{V804M} mutation significantly ($p < 0.001$) increases the affinity of the recombinant receptor for ATP when compared to the recombinant wild type receptor (**Fig. 3E**).

Thus, similar to gatekeeper-induced effects on ATP affinity observed for *EGFR*^{T790M} mutations, our data suggests that these effects may be of relevance for the activity of RET inhibitors in *KIF5B-RET*^{V804M} and *CCDC6-RET*^{V804M} cells (22).

Saturated mutagenesis screening identifies novel *CCDC6-RET*^{I788N} drug resistance mutation

To identify novel RET kinase mutations that may be associated with resistance against targeted therapy we performed accelerated mutagenesis of *RET*-fusion plasmids (23, 24). We identified the *CCDC6-RET*^{I788N} mutation by selection of an AD80 resistant cell population (**Supplementary Table 5**). To validate this finding we engineered Ba/F3 cells expressing *KIF5B-RET*^{I788N} or *CCDC6-RET*^{I788N} and, in fact, observed a

robust shift in cytotoxicity in response to AD80 treatment (**Fig. 4A**), as well as the other RET inhibitors cabozantinib, vandetanib but not ponatinib (**Fig. 4B,C; Fig. S5B**). Immunoblotting confirmed that the introduction of the *KIF5B-RET*^{I788N} mutation had a minor effect on the efficacy of ponatinib but a major impact on AD80 as measured by phospho-RET levels (**Fig. 4D**). Computational binding mode analysis (**Fig. 3C and 4E**) suggests that both positions 804 and 788 are adjacent to the location of AD80's central phenyl ring; characteristic distances between phenyl center of mass and nearest adjacent protein non-hydrogen sites are 4.77 Å to Val804-C(wt), 3.90 Å to Ile788-C(wt), 4.29 Å to Met804-S(V804M), and 4.61 Å to Ile788-C(V804M). However, since V804M and I788N mutants respond differently to AD80, a clear conclusion about the molecular origin is not possible based on structural analysis alone, requiring further investigations.

Thus, our data uncover a novel resistance mutation *RET*^{I788N} that may arise in *RET*-rearranged tumors under RET inhibitor treatment and that retains sensitivity against ponatinib.

Feedback-induced activation of MAPK signaling modulates activity of RET inhibitors

Beyond the acquisition of secondary mutations drug treatment of cancer cells may also lead to the release of feedback loops that override the activity of targeted cancer treatment (25, 26). To systematically characterize these effects we analyzed altered gene expression by RNA-sequencing of LC-2/AD cells under AD80 treatment and performed gene set enrichment analysis (GSEA) (27). Our analyses revealed that treatment with AD80 lead to upregulation of genes that are typically repressed by active KRAS (KRAS down; adj. $p < 0.0001$). On the contrary, genes that are known to

be activated by KRAS were downregulated (KRAS up; adj. $p=0.003$) (**Fig. 5A**). Accordingly, the list of significantly downregulated genes contained *DUSP6* (adj. $p<1\times 10^{-250}$), *SPRY4* (adj. $p=5.75\times 10^{-89}$), *DUSP5* ($2,52\times 10^{-38}$) and other genes that are known to buffer MAPK pathway (**Fig. 5B**). This transcriptional deregulation of MAPK signaling was accompanied by residual phospho-ERK staining in immunoblotting analyses of *RET*-rearranged LC-2/AD cells after 24h of inhibitor treatment (**Fig. S5C**). Using a Group-based Prediction System (GPS 2.12) to identify kinase specific phospho-sites that are perturbed in AD80 treated LC-2/AD cells assessed in our mass-spectrometry based analysis we identified a striking enrichment of phospho-sites known from different families of non-canonical MAPK kinases, such as MAPK8 (66 phospho-sites) MAPK13 (21 phospho-sites) or MAPK12 (15 phospho-sites) (**Fig. 5C**).

We next tested the relevance of RAS-MAPK pathway reactivation in *RET*-rearranged cells and treated with either AD80 alone or a combination of AD80 and the MEK inhibitor trametinib. In TPC-1 cells with limited vulnerability to RET inhibition we observed a pronounced phospho-ERK signal in cells after inhibition with AD80 when compared to LC-2/AD cells (**Fig. S5D**). The combination of AD80 and trametinib fully abrogated MAPK signaling and depleted outgrowth of resistant cells in clonogenic assays and enhanced reduction of viability (**Fig. 5D and Fig. S5E,F**).

To formally test the relevance of MAPK pathway activation in the context of resistance to RET targeted therapies in *RET*-rearranged cells, we stably transduced LC-2/AD cells with lentiviral *KRAS*^{G12V}. Indeed, introduction of the oncogenic *KRAS* allele into LC-2/AD cells largely eliminated activity of AD80 as measured in viability assays and by staining of phospho-ERK (**Fig. 5E,F**).

Overall, our data suggest that drug-induced transcriptional and post-translational reactivation of RAS-MAPK signaling may modulate the activity of RET targeted inhibitors in *RET*-rearranged cells.

AD80 potently shrinks *RET*-rearranged tumors in patient-derived xenografts

To compare the *in vivo* efficacy of AD80 head-to-head with other RET inhibitors we engrafted NIH-3T3 cells driven by CRISPR/Cas9-induced *KIF5B-RET* rearrangements into NSG mice. After development of tumors, mice were treated with either vehicle or 12.5 to 25mg/kg of AD80, cabozantinib or vandetanib and tumors were explanted 4 hours later (28, 29). We observed a pronounced reduction of phosphorylation of RET as well as AKT and ERK in tumors treated with 25mg/kg AD80, but not in tumors treated with cabozantinib or vandetanib (**Fig. 6A**). Encouraged by these results, we next treated a cohort (n=16) of patient-derived xenograft (PDX) mice engrafted with tumor tissue from a *CCDC6-RET* rearranged colorectal cancer (CRC) patient either with vehicle or with 25mg/kg of AD80. Treatment with AD80 induced significant ($p<0.001$) tumor shrinkage in *CCDC6-RET* PDX^{wt} (**Fig. 6B,C; Fig. S6A**) (30). In line with our *in vitro* data of cells harboring *RET* gatekeeper mutations, tumor shrinkage ($p<0.01$) was robust but less pronounced when we treated PDX mice (n=16) engrafted with CRC tissue that had developed a *CCDC6-RET*^{V804M} gatekeeper mutation under ponatinib treatment (**Fig. 6B,D; Fig. S6B**) (31). Consequently, we observed a robust reduction of cellular proliferation (*CCDC6-RET* wt: $p<0.001$; V804M: $p<0.05$) as measured by KI-67 staining in *CCDC6-RET*^{wt} and *CCDC6-RET*^{V804M} tumors (**Fig. 6E,F**). Of importance, AD80 treatment did not lead to body weight loss in both PDX models over the course of the study (**Fig. S6C,D**). Taken together our data indicate that AD80 represents a highly

potent RET inhibitor with a favorable pharmacokinetic profile in clinically relevant *RET* fusion driven tumor models.

Discussion

Our chemical-genomic and chemical-proteomic analyses revealed three interesting findings with major implications for the development of effective therapies against *RET*-rearranged tumors: i) *RET*-rearranged tumors show exquisite vulnerability to a subset of type II inhibitors that target the DFG-out conformation of RET kinase, ii) compound specificity and compound activity can be only faithfully determined in orthogonal *in vitro* and *in vivo* models of rearranged RET and iii) resistance mechanisms against targeted inhibition of RET may involve *RET*^{T788N} mutations and the reactivation of MAPK signaling.

The repurposing of crizotinib for the targeted treatment of *ALK*-rearranged tumors enabled a fast-track introduction of precision cancer medicine for this group of cancer patients and raised hopes that this approach may be a blueprint for the targeted treatment of other driver oncogenes, such as RET (32). Although initial clinical response rates were promising in selected patients, a median progression-free survival of less than 6 months and response rates of only about 18% in retrospective studies indicated that *RET* may be a difficult drug target after all (7-9, 33). These data are in line with our own retrospective analysis where out of four patients with *RET*-rearranged tumors we observed only one PR in a patient receiving vandetanib (P2) as first-line treatment (**Fig. S7, Supplementary Table 6A,B**). Interestingly, sequencing of rebiopsy samples did not reveal candidate drug resistance mutations, suggesting that the target had been insufficiently inhibited (**Supplementary Methods; Supplementary Table 6C**).

Our systematic characterization of anti-RET drugs revealed unique activity and specificity profiles for the type II kinase inhibitors AD80 and ponatinib across orthogonal *in vitro* and *in vivo* models across different lineages of *RET*-rearranged cancer. This finding is noteworthy, since the biochemical profiling of these compounds and structurally related compounds would have suggested a broad spectrum of kinase targets (12, 34, 35). Our data also suggest that a tight RET inhibitor binding in the DFG-out conformation of RET as measured by thermal shift assays only partially tracks with potent *in vitro* kinase activity and that an optimal combination of both drug target interactions may open up a unique opportunity for an effective inhibition of RET signaling. It remains to be seen how much drug residence time or structural kinetics that capture additional features of drug target interactions may contribute to the overall activity of type II inhibitors like sorafenib and other RET inhibitors (19, 36).

Of note, we identify a novel *CCDC6-RET*^{T788N} resistance mutation that renders a number of tested RET inhibitors ineffective while retaining vulnerability against ponatinib. These findings resemble the experience with ALK inhibitors in *ALK*-rearranged tumors where the availability of potent inhibitors allows a mutant specific selection of inhibitors to overcome drug resistance (37). In addition, our results suggest that the reactivation of intracellular networks including MAPK signaling may contribute to drug tolerance and over time may modulate the efficacy of RET kinase inhibitors in *RET*-rearranged tumors. Given the evident clinical need for effective targeted drugs against RET our results provide a strong rationale for optimization of current therapeutic strategies and development of RET inhibitors for an effective treatment of *RET*-rearranged cancers.

Materials and Methods

CRISPR/Cas9

CRISPR technology was used via a pLenti vector containing Cas9-IRES-blasticidine and two U6 promoters for expression of individual sgRNAs (sgRNA1 (intron 15 murine *KIF5B*): *GGCACCAAACACTTCACCCC*; sgRNA2 (intron 11 murine *RET*): *GGGTGTAGCGAAGTGTGCAT*) (14). 24 hours after transfection the media was changed to media supplemented with blasticidine (10µg/ml) (Life Technologies) for 4 days.

Immunoblot analyses

Immunoblot analyses were performed as previously described (38). The individual antibodies are specified in the Supplementary Data. Detections of proteins was performed via horseradish peroxidase or via near-infrared fluorescent antibodies using a LI-COR Odyssey® CLx imaging system.

Phosphoproteomic analyses

LC-2/AD cells were treated with 0, 10 or 100 nM AD80, lysed, proteolytically digested with Trypsin and labeled with an Isobaric Mass Tag (TMT10plex, Thermo Fisher Scientific). Peptides for global proteome analysis were fractionated by high-pH reversed phase chromatography. Phosphopeptides were enriched via TiO₂ beads and fractionated using hydrophilic interaction chromatography (39). Fractions were analyzed by nano LC-MS/MS on a Q-Exactive HF mass spectrometer (Thermo Scientific) and data were analyzed using the Proteome Discoverer 1.4 software (Thermo Scientific).

Protein Thermal Shift assay

Different variants of RET kinase domain were designed and ordered from Genart (Life Technologies). RET variants were expressed in SF21 cells and harvested 72h post transfection. Subsequently proteins were purified and phosphorylated. For determining the protein thermal shift protein variants were incubated with DMSO or 1 μ M compound. Sypro-Orange dye (Life Technologies) was added to each drug treatment and thermal shift was measured in a 7500 Fast RT PCR machine (Applied Biosystems) in a temperature range of 25 – 90°C. Subsequent analysis was performed using Protein Thermal Shift Software v1.2 (Applied Biosystems).

Computational binding mode modeling

Briefly, the VEGFR was taken as template for modeling and filling of sequence gaps, representing the relevant part of the wt RET protein. All ligand-bound models were created by superpositioning followed by extensive MD simulations and energy minimization to relax the structures (RET^{wt}/AD80, RET^{V804M}/AD80, RET^{wt}/Cabozantinib). For comparison with experimentally determined IC₅₀ ratios, the binding free energy difference between RET^{wt}/AD80 and RET^{wt}/AD57 was further estimated by MD simulations and integral equation calculations (40), the latter approach was also used for approximate determination of the impact of the V804M mutation on the binding affinity of AD80. A detailed description can be found in the supplementary methods section.

ATP binding constant determination

ATP K_m determination for RET wt and V804M mutant was performed using the HTRF KinEASE-TK assay (Cisbio) according to manufacturer's instructions. To

determine ATP K_m , wt and V804M mutant were incubated with different ATP concentrations (300 μ M - 1.7nM) for 20min (RET^{wt}) and 15min (RET^{V804M}). Phosphorylation of the substrate peptide was determined by FRET between europium cryptate and XL665. ATP K_m (app) was calculated using a Michaelis-Menten plot.

PDX

Tumor fragments from stock mice inoculated with *CCDC6-RET* fusion positive patient-derived tumor tissues were harvested and used for inoculation into BALB/c nude mice. Mice were randomly allocated into vehicle and AD80 (25mg/kg) treated groups when the average tumor volume reached 100-200mm³. Tumor volume was measured twice weekly in two dimensions using a caliper, and the volume is expressed in mm³ (TV = 0.5 a \times b², a/b represent long and short diameter).

Immunohistochemistry

Immunohistochemistry was performed on Leica Bond automated staining systems using Ki-67 and Mib-1 (Dako) antibodies according to the manufacturer's instructions. Ki-67 labeling index was determined by manually counting 100 tumor cells in the area of the highest proliferation.

Supplementary Materials

Supplementary Materials and Methods

Methods

Fig. S1. Selective inhibition of signaling induced by rearranged RET.

Fig. S2. Characterization of the activity profile of AD80.

Fig. S3. Delineation of the cellular targets of AD80 using ligand screens and thermal shift experiments and comparison of type I and II RET kinase inhibitors.

Fig. S4. Root mean square deviations (RMSD) measurements of RET and AD80 or cabozantinib and optimized structures after extensive MD refinement followed by ALPB optimization.

Fig. S5. Inhibitory potential of AD80 derivatives and primary and secondary resistance against RET inhibition.

Fig. S6. Validation of PDX via FISH and *in vivo* effects induced by treatment with AD80.

Fig. S7. Limited clinical activity of currently available RET inhibitors and validation of a small cohort of patients with *RET*-rearrangements.

Table S1. IC₅₀ values of AD80, cabozantinib and vandetanib for phospho-RET levels in Ba/F3 cells expressing wild type or V804M *KIF5B-RET*.

Table S2. GI₅₀ values of the panel of patient-derived cell lines.

Table S3. Tabulated derivative melting temperatures (T_m) and differences in melting temperature (ΔT_m) values.

Table S4. *In vitro* kinase assay of RET wt, V804M and V804L mutants with different inhibitors.

Table S5. Experimental setup for saturated mutagenesis screening.

Table S6. Clinical response rates to currently available anti-RET drugs and clinical information of patients used in retrospective analysis.

References (41-64)

References and Notes

1. D. Lipson, M. Capelletti, R. Yelensky, G. Otto, A. Parker, M. Jarosz, J. A. Curran, S. Balasubramanian, T. Bloom, K. W. Brennan, A. Donahue, S. R. Downing, G. M. Frampton, L. Garcia, F. Juhn, K. C. Mitchell, E. White, J. White, Z. Zwirko, T. Peretz, H. Nechushtan, L. Soussan-Gutman, J. Kim, H. Sasaki, H. R. Kim, S.-I. Park, D. Ercan, C. E. Sheehan, J. S. Ross, M. T. Cronin, P. A. Jänne, P. J. Stephens, Identification of new ALK and RET gene fusions from colorectal and lung cancer biopsies, *Nat. Med.* **18**, 382–384 (2012).
2. K. Takeuchi, M. Soda, Y. Togashi, R. Suzuki, S. Sakata, S. Hatano, R. Asaka, W. Hamanaka, H. Ninomiya, H. Uehara, Y. Lim Choi, Y. Satoh, S. Okumura, K. Nakagawa, H. Mano, Y. Ishikawa, RET, ROS1 and ALK fusions in lung cancer, *Nat. Med.* **18**, 378–381 (2012).
3. T. Kohno, H. Ichikawa, Y. Totoki, K. Yasuda, M. Hiramoto, T. Nammo, H. Sakamoto, K. Tsuta, K. Furuta, Y. Shimada, R. Iwakawa, H. Ogiwara, T. Oike, M. Enari, A. J. Schetter, H. Okayama, A. Haugen, V. Skaug, S. Chiku, I. Yamanaka, Y. Arai, S.-I. Watanabe, I. Sekine, S. Ogawa, C. C. Harris, H. Tsuda, T. Yoshida, J. Yokota, T. Shibata, KIF5B-RET fusions in lung adenocarcinoma, *Nat. Med.* **18**, 375–377 (2012).
4. T. Kodama, T. Tsukaguchi, Y. Satoh, M. Yoshida, Y. Watanabe, O. Kondoh, H. Sakamoto, Alectinib shows potent antitumor activity against RET-rearranged non-small cell lung cancer, *Molecular Cancer Therapeutics* **13**, 2910–2918 (2014).
5. R. Kurzrock, S. I. Sherman, D. W. Ball, A. A. Forastiere, R. B. Cohen, R. Mehra, D. G. Pfister, E. E. W. Cohen, L. Janisch, F. Nauling, D. S. Hong, C. S. Ng, L. Ye, R. F. Gagel, J. Frye, T. Müller, M. J. Ratain, R. Salgia, Activity of XL184 (Cabozantinib), an oral tyrosine kinase inhibitor, in patients with medullary thyroid cancer, *J. Clin. Oncol.* **29**, 2660–2666 (2011).
6. M. G. Borrello, E. Ardini, L. D. Locati, A. Greco, L. Licitra, M. A. Pierotti, RET inhibition: implications in cancer therapy, *Expert Opinion on Therapeutic Targets* **17**, 403–419 (2013).
7. O. Gautschi, J. Wolf, J. Milia, T. Filleron, D. P. Carbone, D. R. Camidge, J.-Y. Shih, M. M. Awad, F. Cabillic, N. Peled, M. van den Heuvel, D. H. Owen, M. G. Kris, P. A. Jänne, B. Besse, B. C. Cho, D. D. Karp, R. Rosell, J. Mazieres, A. E. Drilon, Targeting RET in patients with *RET*-rearranged lung cancers: Results from a global registry. meetinglibrary.asco.org (2016).
8. A. Drilon, L. Wang, A. Hasanovic, Y. Suehara, D. Lipson, P. Stephens, J. Ross, V. Miller, M. Ginsberg, M. F. Zakowski, M. G. Kris, M. Ladanyi, N. Rizvi, Response to Cabozantinib in patients with RET fusion-positive lung adenocarcinomas, *Cancer*

Discovery **3**, 630–635 (2013).

9. K. Yoh, T. Seto, M. Satouchi, M. Nishio, N. Yamamoto, H. Murakami, N. Nogami, S. Matsumoto, T. Kohno, K. Tsuta, K. Tsuchihara, G. Ishii, S. Nomura, A. Sato, A. Ohtsu, Y. Ohe, K. Goto, Vandetanib in patients with previously treated RET-rearranged advanced non-small-cell lung cancer (LURET): an open-label, multicentre phase 2 trial, *The Lancet Respiratory Medicine* **5**, 42–50 (2017).

10. G. S. Falchook, N. G. Ordóñez, C. C. Bastida, P. J. Stephens, V. A. Miller, L. Gaido, T. Jackson, D. D. Karp, Effect of the RET Inhibitor Vandetanib in a Patient With RET Fusion-Positive Metastatic Non-Small-Cell Lung Cancer, *Journal of Clinical Oncology* (2016), doi:10.1200/JCO.2013.50.5016;page:string:Article/Chapter.

11. T. Cascone, K. R. Hess, S. Piha-Paul, D. S. Hong, I. M. Subblah, T. Bhatt, A. Lui, S. Fu, A. Naing, F. Janku, D. D. Karp, F. Meric-Bernstam, J. V. Heymach, V. Subblah, Safety, toxicity and activity of multi-kinase inhibitor vandetanib in combination with everolimus in advanced solid tumors. *meetinglibrary.asco.org* (2016).

12. A. C. Dar, T. K. Das, K. M. Shokat, R. L. Cagan, Chemical genetic discovery of targets and anti-targets for cancer polypharmacology, *Nature* **486**, 80–84 (2012).

13. M. Song, Progress in Discovery of KIF5B-RET Kinase Inhibitors for the Treatment of Non-Small-Cell Lung Cancer, *J. Med. Chem.* **58**, 3672–3681 (2015).

14. P. S. Choi, M. Meyerson, Targeted genomic rearrangements using CRISPR/Cas technology, *Nature Communications* **5**, 3728 (2014).

15. M. Suzuki, H. Makinoshima, S. Matsumoto, A. Suzuki, S. Mimaki, K. Matsushima, K. Yoh, K. Goto, Y. Suzuki, G. Ishii, A. Ochiai, K. Tsuta, T. Shibata, T. Kohno, H. Esumi, K. Tsuchihara, Identification of a lung adenocarcinoma cell line with CCDC6-RET fusion gene and the effect of RET inhibitors in vitro and in vivo, *Cancer Science* **104**, 896–903 (2013).

16. M. L. Sos, K. Michel, T. Zander, J. Weiss, P. Frommolt, M. Peifer, D. Li, R. Ullrich, M. Koker, F. Fischer, T. Shimamura, D. Rauh, C. Mermel, S. Fischer, I. Stückrath, S. Heynck, R. Beroukhim, W. Lin, W. Winckler, K. Shah, T. LaFramboise, W. F. Moriarty, M. Hanna, L. Tolosi, J. Rahnenführer, R. Verhaak, D. Chiang, G. Getz, M. Hellmich, J. Wolf, L. Girard, M. Peyton, B. A. Weir, T.-H. Chen, H. Greulich, J. Barretina, G. I. Shapiro, L. A. Garraway, A. F. Gazdar, J. D. Minna, M. Meyerson, K.-K. Wong, R. K. Thomas, Predicting drug susceptibility of non-small cell lung cancers based on genetic lesions, *J. Clin. Invest.* **119**, 1727–1740 (2009).

17. P. P. Knowles, J. Murray-Rust, S. Kjær, R. P. Scott, S. Hanrahan, M. Santoro, C. F. Ibáñez, N. Q. McDonald, Structure and chemical inhibition of the RET tyrosine kinase domain, *J. Biol. Chem.* **281**, 33577–33587 (2006).

18. Masaichi Hasegawa, Naohiko Nishigaki, Yoshiaki Washio, Kazuya Kano, Philip A Harris, Hideyuki Sato, Ichiro Mori, Rob I West, Megumi Shibahara, Hiroko Toyoda, Liping Wang, Robert T Nolte, A. James M Veal, M. Cheung, Discovery of Novel Benzimidazoles as Potent Inhibitors of TIE-2 and VEGFR-2 Tyrosine Kinase

Receptors, *J. Med. Chem.* **50**, 4453–4470 (2007).

19. B. Frett, F. Carlomagno, M. L. Moccia, A. Brescia, G. Federico, V. De Falco, B. Admire, Z. Chen, W. Qi, M. Santoro, H. Y. Li, Fragment-Based Discovery of a Dual pan-RET/VEGFR2 Kinase Inhibitor Optimized for Single-Agent Polypharmacology, *Angewandte Chemie International Edition* **54**, 8717–8721 (2015).

20. F. Carlomagno, T. Guida, S. Anaganti, G. Vecchio, A. Fusco, A. J. Ryan, M. Billaud, M. Santoro, Disease associated mutations at valine 804 in the RET receptor tyrosine kinase confer resistance to selective kinase inhibitors, *Oncogene* **23**, 6056–6063 (2004).

21. L. Mologni, S. Redaelli, A. Morandi, I. Plaza-Menacho, C. Gambacorti-Passerini, Ponatinib is a potent inhibitor of wild-type and drug-resistant gatekeeper mutant RET kinase, *Molecular and Cellular Endocrinology* **377**, 1–6 (2013).

22. C.-H. Yun, K. E. Mengwasser, A. V. Toms, M. S. Woo, H. Greulich, K.-K. Wong, M. Meyerson, M. J. Eck, The T790M mutation in EGFR kinase causes drug resistance by increasing the affinity for ATP, *Proc. Natl. Acad. Sci. U.S.A.* **105**, 2070–2075 (2008).

23. M. Azam, R. R. Latek, G. Q. Daley, Mechanisms of Autoinhibition and STI-571/Imatinib Resistance Revealed by Mutagenesis of BCR-ABL, *Cell* **112**, 831–843 (2003).

24. J. M. Heuckmann, M. Holzel, M. L. Sos, S. Heynck, H. Balke-Want, M. Koker, M. Peifer, J. Weiss, C. M. Lovly, C. Grutter, D. Rauh, W. Pao, R. K. Thomas, ALK Mutations Conferring Differential Resistance to Structurally Diverse ALK Inhibitors, *Clinical Cancer Research* **17**, 7394–7401 (2011).

25. M. L. Sos, R. S. Levin, J. D. Gordan, J. A. Oses-Prieto, J. T. Webber, M. Salt, B. Hann, A. L. Burlingame, F. McCormick, S. Bandyopadhyay, K. M. Shokat, Oncogene Mimicry as a Mechanism of Primary Resistance to BRAF Inhibitors, *Cell Rep* **8**, 1037–1048 (2014).

26. S. Chandarlapaty, Negative Feedback and Adaptive Resistance to the Targeted Therapy of Cancer, *Cancer Discovery* **2**, 311–319 (2012).

27. A. Subramanian, P. Tamayo, V. K. Mootha, S. Mukherjee, B. L. Ebert, M. A. Gillette, A. Paulovich, S. L. Pomeroy, T. R. Golub, E. S. Lander, J. P. Mesirov, Gene set enrichment analysis: a knowledge-based approach for interpreting genome-wide expression profiles, *PNAS* **102**, 15545–15550 (2005).

28. R. de Boer, Y. Humblet, J. Wolf, L. Nogová, K. Ruffert, T. Milenkova, R. Smith, A. Godwood, J. Vansteenkiste, An open-label study of vandetanib with pemetrexed in patients with previously treated non-small-cell lung cancer, *Ann. Oncol.* **20**, 486–491 (2009).

29. F. Bentzien, M. Zuzow, N. Heald, A. Gibson, Y. Shi, L. Goon, P. Yu, S. Engst, W. Zhang, D. Huang, L. Zhao, V. Vysotskaia, F. Chu, R. Bautista, B. Cancilla, P. Lamb, A. H. Joly, F. M. Yakes, In vitro and in vivo activity of cabozantinib (XL184), an

- inhibitor of RET, MET, and VEGFR2, in a model of medullary thyroid cancer, *Thyroid* **23**, 1569–1577 (2013).
30. J. M. Gozgit, T.-H. Chen, T. Clackson, V. M. Rivera, Abstract 2726: RET fusions identified in colorectal cancer PDX models are sensitive to the potent RET inhibitor ponatinib, *Cancer Research* **74**, 2726–2726 (2014).
31. M. Yang, J. Cai, S. Guo, J.-P. Wery, H. Q. Li, Abstract 3581: Rapid conversion to resistance, of a colon PDX with ret-fusion, by ponatinib treatment could potentially be attributed to the introduction of the gate keeper mutation V804M, *Cancer Research* **75**, 3581–3581 (2015).
32. B. J. Solomon, T. Mok, D.-W. Kim, Y.-L. Wu, K. Nakagawa, T. Mekhail, E. Felip, F. Cappuzzo, J. Paolini, T. Usari, S. Iyer, A. Reisman, K. D. Wilner, J. Tursi, F. Blackhall, First-Line Crizotinib versus Chemotherapy in ALK-Positive Lung Cancer, *N. Engl. J. Med.* **371**, 2167–2177 (2014).
33. O. Gautschi, T. Zander, F. A. Keller, K. Strobel, A. Hirschmann, S. Aebi, J. Diebold, A Patient with Lung Adenocarcinoma and RET Fusion Treated with Vandetanib, *Journal of Thoracic Oncology* **8**, e43–e44 (2013).
34. A. C. Dar, M. S. Lopez, K. M. Shokat, Small Molecule Recognition of c-Src via the Imatinib-Binding Conformation, *Chemistry & Biology* **15**, 1015–1022 (2008).
35. T. O'Hare, W. C. Shakespeare, X. Zhu, C. A. Eide, V. M. Rivera, F. Wang, L. T. Adrian, T. Zhou, W.-S. Huang, Q. Xu, C. A. Metcalf III, J. W. Tyner, M. M. Loriaux, A. S. Corbin, S. Wardwell, Y. Ning, J. A. Keats, Y. Wang, R. Sundaramoorthi, M. Thomas, D. Zhou, J. Snodgrass, L. Commodore, T. K. Sawyer, D. C. Dalgarno, M. W. N. Deininger, B. J. Druker, T. Clackson, AP24534, a Pan-BCR-ABL Inhibitor for Chronic Myeloid Leukemia, Potently Inhibits the T315I Mutant and Overcomes Mutation-Based Resistance, *Cancer Cell* **16**, 401–412 (2009).
36. F. Carlomagno, S. Anaganti, T. Guida, G. Salvatore, G. Troncone, S. M. Wilhelm, M. Santoro, BAY 43-9006 Inhibition of Oncogenic RET Mutants, *J. Natl. Cancer Inst.* **98**, 326–334 (2006).
37. J. F. Gainor, L. Dardaei, S. Yoda, L. Friboulet, I. Leshchiner, R. Katayama, I. Dagogo-Jack, S. Gadgeel, K. Schultz, M. Singh, E. Chin, M. Parks, D. Lee, R. H. DiCecca, E. Lockerman, T. Huynh, J. Logan, L. L. Ritterhouse, L. P. Le, A. Muniappan, S. Digumarthy, C. Channick, C. Keyes, G. Getz, D. Dias-Santagata, R. S. Heist, J. Lennerz, L. V. Sequist, C. H. Benes, A. J. Iafrate, M. Mino-Kenudson, J. A. Engelman, A. T. Shaw, Molecular Mechanisms of Resistance to First- and Second-Generation ALK Inhibitors in ALK-Rearranged Lung Cancer, *Cancer Discovery* **6**, 1118–1133 (2016).
38. L. Fernandez-Cuesta, D. Plenker, H. Osada, R. Sun, R. Menon, F. Leenders, S. Ortiz-Cuaran, M. Peifer, M. Bos, J. Daßler, F. Malchers, J. Schottle, W. Vogel, I. Dahmen, M. Koker, R. T. Ullrich, G. M. Wright, P. A. Russell, Z. Wainer, B. Solomon, E. Brambilla, H. Nagy-Mignotte, D. Moro-Sibilot, C. G. Brambilla, S. Lantuejoul, J. Altmuller, C. Becker, P. Nurnberg, J. M. Heuckmann, E. Stoelben, I. Petersen, J. H. Clement, J. Sanger, L. A. Muscarella, A. la Torre, V. M. Fazio, I.

- Lahortiga, T. Perera, S. Ogata, M. Parade, D. Brehmer, M. Vingron, L. C. Heukamp, R. Buettner, T. Zander, J. Wolf, S. Perner, S. Ansén, S. A. Haas, Y. Yatabe, R. K. Thomas, CD74-NRG1 Fusions in Lung Adenocarcinoma, *Cancer Discovery* **4**, 415–422 (2014).
39. C. Dickhut, S. Radau, R. P. Zahedi, Fast, efficient, and quality-controlled phosphopeptide enrichment from minute sample amounts using titanium dioxide, *Methods Mol. Biol.* **1156**, 417–430 (2014).
40. J. Heil, S. M. Kast, 3D RISM theory with fast reciprocal-space electrostatics, *The Journal of Chemical Physics* **142**, 114107 (2015).
41. J. R. Wiśniewski, A. Zougman, N. Nagaraj, M. Mann, Universal sample preparation method for proteome analysis, *Nat Meth* **6**, 359–362 (2009).
42. L. Kollipara, R. P. Zahedi, R. Zahedi, A. Sickmann, Eds. Protein carbamylation: In vivo modification or in vitro artefact? *PROTEOMICS* **13**, 941–944 (2013).
43. J. M. Burkhardt, C. Schumbrutzki, S. Wortelkamp, A. Sickmann, R. P. Zahedi, Systematic and quantitative comparison of digest efficiency and specificity reveals the impact of trypsin quality on MS-based proteomics, *Journal of Proteomics* **75**, 1454–1462 (2012).
44. K. Engholm-Keller, P. Birck, J. Størling, F. Pociot, T. Mandrup-Poulsen, M. R. Larsen, TiSH — a robust and sensitive global phosphoproteomics strategy employing a combination of TiO₂, SIMAC, and HILIC, *Journal of Proteomics* **75**, 5749–5761 (2012).
45. T. Taus, T. Köcher, P. Pichler, C. Paschke, A. Schmidt, C. Henrich, K. Mechtler, Universal and Confident Phosphorylation Site Localization Using phosphoRS, *J. Proteome Res.* **10**, 5354–5362 (2011).
46. M. Spivak, J. Weston, L. Bottou, L. Käll, W. S. Noble, Improvements to the Percolator Algorithm for Peptide Identification from Shotgun Proteomics Data Sets, *J. Proteome Res.* **8**, 3737–3745 (2009).
47. Y. Xue, J. Ren, X. Gao, C. Jin, L. Wen, X. Yao, GPS 2.0, a tool to predict kinase-specific phosphorylation sites in hierarchy, *Mol Cell Proteomics* **7**, 1598–1608 (2008).
48. *modelleralilab.org* (available at <https://salilab.org/modeller/>).
49. G. Sigalov, A. Fenley, A. Onufriev, Analytical electrostatics for biomolecules: Beyond the generalized Born approximation, *The Journal of Chemical Physics* **124**, 124902 (2006).
50. *Amberambermd.org*, doi:10.1002/jcc.23031/abstract.
51. J. Engel, A. Richters, M. Getlik, S. Tomassi, M. Keul, M. Termathe, J. Lategahn, C. Becker, S. Mayer-Wrangowski, C. Grütter, N. Uhlenbrock, J. Krüll, N. Schaumann, S. Eppmann, P. Kibies, F. Hoffgaard, J. Heil, S. Menninger, S. Ortiz-Cuaran, J. M. Heuckmann, V. Tinnfeld, R. P. Zahedi, M. L. Sos, C. Schultz-Fademrecht, R. K. Thomas, S. M. Kast, D. Rauh, Targeting Drug Resistance in EGFR with Covalent

- Inhibitors: A Structure-Based Design Approach, *J. Med. Chem.* **58**, 6844–6863 (2015).
52. W. L. Jorgensen, J. Chandrasekhar, J. D. Madura, R. W. Impey, M. L. Klein, Comparison of simple potential functions for simulating liquid water, *The Journal of Chemical Physics* **79**, 926–935 (1983).
53. NAMDKs.uiuc.edu, doi:10.1002/jcc.23422/abstract.
54. salilab.org (; <https://salilab.org>).
55. D. Beglov, B. Roux, An Integral Equation To Describe the Solvation of Polar Molecules in Liquid Water, *J. Phys. Chem. B* **101**, 7821–7826 (1997).
56. A. Kovalenko, F. Hirata, Three-dimensional density profiles of water in contact with a solute of arbitrary shape: a RISM approach, *Chemical Physics Letters* **290**, 237–244 (1998).
57. F. Mrugalla, S. M. Kast, Designing molecular complexes using free-energy derivatives from liquid-state integral equation theory, *J. Phys.: Condens. Matter* **28**, 344004 (2016).
58. C. Trapnell, L. Pachter, S. L. Salzberg, TopHat: discovering splice junctions with RNA-Seq, *Bioinformatics* **25**, 1105–1111 (2009).
59. M. Lawrence, W. Huber, H. Pagès, P. Aboyoun, M. Carlson, R. Gentleman, M. T. Morgan, V. J. Carey, A. Prlic, Ed. Software for Computing and Annotating Genomic Ranges, *PLoS Comput Biol* **9**, e1003118 (2013).
60. M. I. Love, W. Huber, S. Anders, Moderated estimation of fold change and dispersion for RNA-seq data with DESeq2, *Genome Biol* **15**, 31 (2014).
61. A. Liberzon, C. Birger, H. Thorvaldsdóttir, M. Ghandi, J. P. Mesirov, P. Tamayo, The Molecular Signatures Database (MSigDB) hallmark gene set collection, *Cell Syst* **1**, 417–425 (2015).
62. V. K. Mootha, C. M. Lindgren, K.-F. Eriksson, A. Subramanian, S. Sihag, J. Lehár, P. Puigserver, E. Carlsson, M. Ridderstråle, E. Laurila, N. Houstis, M. J. Daly, N. Patterson, J. P. Mesirov, T. R. Golub, P. Tamayo, B. Spiegelman, E. S. Lander, J. N. Hirschhorn, D. Altshuler, L. C. Groop, PGC-1[α]-responsive genes involved in oxidative phosphorylation are coordinately downregulated in human diabetes, *Nat Genet* **34**, 267–273 (2003).
63. M. W. Karaman, S. Herrgard, D. K. Treiber, P. Gallant, C. E. Atteridge, B. T. Campbell, K. W. Chan, P. Ciceri, M. I. Davis, P. T. Edeen, R. Faraoni, M. Floyd, J. P. Hunt, D. J. Lockhart, Z. V. Milanov, M. J. Morrison, G. Pallares, H. K. Patel, S. Pritchard, L. M. Wodicka, P. P. Zarrinkar, A quantitative analysis of kinase inhibitor selectivity, *Nat Biotechnol* **26**, 127–132 (2008).
64. M. I. Davis, J. P. Hunt, S. Herrgard, P. Ciceri, L. M. Wodicka, G. Pallares, M. Hocker, D. K. Treiber, P. P. Zarrinkar, Comprehensive analysis of kinase inhibitor selectivity, *Nat Biotechnol* **29**, 1046–1051 (2011).

Acknowledgements: We thank Dr. Thomas Zillinger from the University Hospital Bonn for sharing the Cas9 expression and the backbone of the pLenti-IRES-blasticidine vector system, the members of the Sos lab and Thomas lab for technical support, Alexandra Florin and Ursula Rommerscheidt-Fuß for supporting us with IHC staining and Patrick Kibies and Lukas Eberlein as well as Ludger Goeminne and Lieven Clement for supporting the computational modeling. We thank AstraZeneca (Zug, Switzerland) for supporting vandetanib off label use, SOBI (Lyngby, Denmark) for providing cabozantinib compassionate use, and Franziska Aebersold and Astrid Hirschmann (Luzern, Switzerland) for diagnostic work.

Funding: This work was supported by the German federal state North Rhine Westphalia (NRW) and by the European Union (European Regional Development Fund: Investing In Your Future) as part of the PerMed.NRW initiative (grant 005-1111-0025 to R.K.T., J.W. and R.B) as well as the EFRE initiative (grant LS-1-1-030 to R.B., J.W., R.K.T. and M.L.S) and by the German Ministry of Science and Education (BMBF) as part of the e:Med program (grant no. 01ZX1303 to M.P. and 01ZX1603, R.K.T., J.W., R.B and grant no. 01ZX1406 to M.P. and M.L.S), by the Deutsche Forschungsgemeinschaft (DFG; through TH1386/3-1 to R.K.T and M.L.S. and KA1381/5-1 to S.M.K) and by the German Consortium for Translational Cancer Research (DKTK) Joint Funding program. V.T. is the recipient of a joint ERS/EMBO Long-Term Research fellowship n° LTRF 2014-2951. N.Q.M. acknowledges that this work was supported by the Francis Crick Institute, which receives its core funding from Cancer Research UK (FC001115), the UK Medical Research Council (FC001115) and the Wellcome Trust (FC001115); by the NCI/NIH (grant reference 5R01CA197178); by the Association for Multiple Endocrine Neoplasia

Disorders MTC Research Fund. Financial support by the Ministerium für Innovation, Wissenschaft und Forschung des Landes Nordrhein-Westfalen, the Senatsverwaltung für Wirtschaft, Technologie und Forschung des Landes Berlin (O.P., R.P.Z.) and the Bundesministerium für Bildung und Forschung (O.P., R.P.Z.) is gratefully acknowledged.

Authors' Contribution: D.P., M.R., J.B., M.D., C.L. and D.S. performed the cloning, experiments and cell culture experiments. V.T., A.H.S. and R.B. analyzed IHC and FISH images. Y.S. was responsible for PDX establishment and measurements. J. S., F.M., Y.A. and S.M.K performed computational modeling. O.P. and R.P.Z. performed quantitative phosphoproteomics and data analysis. M.K., M.B., A.R., J.S., J.E., M.A. and K.G. performed *in vitro* kinase experiments and analyses. R.C., P.P.K, and N.Q.M. purified recombinant RET fusion proteins and carried out the thermal shift analyses. J.D., G.P. and O.G. contributed the clinical patient data. F.L. and J.M.H. were responsible for NGS of RET. J.B. and M.P. analyzed RNAseq data. K.M.S. provided compounds. D.P., M.R., J.B., M.D., F.L., J.W., N.Q.M., K.M.S., R.K.T and M.L.S. interpreted the data and performed statistical analyses. D.P., M.R., S.M.K., R.K.T., O.G. and M.L.S. wrote the manuscript.

Competing interest: R.K.T. is a founder and consultant of NEO New Oncology GmbH, received commercial research grants from AstraZeneca, EOS and Merck KgaA and honoraria from AstraZeneca, Bayer, NEO New Oncology AG, Boehringer Ingelheim, Clovis Oncology, Daiichi-Sankyo, Eli Lilly, Johnson & Johnson, Merck KgaA, MSD, Puma, Roche and Sanofi. F.L. and J.M.H. are employee of NEO New Oncology GmbH. M.L.S received commercial research grants from Novartis. K.M.S and M.L.S. are both patent holders for the compound AD80.

Data and materials availability: RNA-seq data was deposited at the European Genome-phenome Archive (<https://www.ebi.ac.uk/ega/>, accession number EGAS00001002335). The mass spectrometry proteomics data have been deposited to the ProteomeXchange Consortium via the PRIDE partner repository with the dataset identifier PXD006006.

Figures

Figure 1

A) Dose-response curves (72h) as assessed for AD80, cabozantinib (CAB), vandetanib (VAN), alectinib (ALE), regorafenib (REG), sorafenib (SOR), ponatinib (PON), crizotinib (CRI), ceritinib (CER) or PF06463922 (PF06) in *KIF5B-RET* expressing Ba/F3 cells. **B)** Immunoblotting results of *KIF5B-RET* rearranged Ba/F3 cells after treatment are displayed (4h). **C)** Relative mean colony number of NIH-3T3 cells engineered with *KIF5B-RET* fusion via CRISPR/Cas9 was assessed in soft agar assays after 7 days under treatment. Representative pictures of colonies under AD80 treatment are depicted in the lower panel. Black bar is equal to 100 μ m. **D)** Immunoblotting of treated CRISPR/Cas9 engineered *KIF5B-RET*-rearranged NIH-3T3 cells with AD80, cabozantinib or vandetanib (4h). *KIF5B-RET* expressing Ba/F3 cells (Ba/F3 ctrl.) serve as control for RET signaling. **E)** Dose-response curves (72h) as assessed for different inhibitors in LC-2/AD cells are shown. **F)** Immunoblotting was performed in LC-2/AD cells treated with AD80, cabozantinib or vandetanib (4h).

Figure 2

A) Scatter plot of log₂-fold phosphorylation change for LC-2/AD cells treated (4h) with either 10nM or 100nM AD80. Each dot represents a single phospho-site;

phospho-RET (Y900) is highlighted in red. **B)** Difference in melting temperatures after AD80, sorafenib (SOR), vandetanib (VAN) or sunitinib (SUN) addition (ΔT_m) and the respective standard errors of the mean (SEM) are shown for each construct. Thermal shift experiments were performed using independent preparations of each protein and were carried out in triplicates (left panel). Representative thermal melting curves for Δ KIF5B-KD incubated with either AD80 (1 μ M) or the equivalent volume of DMSO (ctrl.) are shown (right panel).

Figure 3

A) Optimized structures after extensive MD refinement followed by ALPB optimization. (I) RET-wt/AD80 after 102 ns, (II) RET-wt/AD57 after 202 ns (92 ns from RET-wt/AD80 simulation followed by 110 ns TI-MD), (III) RET-V804M/AD80 after 107 ns (side view). The DFG motif is shown in violet. Distances from central phenyl's center: 4.77 Å to Val804-C(wt), 3.90 Å to Ile788-C(wt) and 4.29 Å to Met804-S(V804M). Dashed lines indicate the marked H-bond between the bound ligands and aspartate of the DFG motif. **B)** Heatmap of mean GI_{50} -values (from $n \geq 3$) of Ba/F3 cells expressing CCDC6-RET^{V804M} or KIF5B-RET^{V804M} after 72h of treatment as assessed for various inhibitors is shown. **C)** Immunoblotting of AD80, cabozantinib or vandetanib treated (4h) KIF5B-RET^{V804M} Ba/F3 cells is displayed. **D)** Immunoblotting of Ba/F3 cells expressing CCDC6-RET-RET^{wt} or CCDC6-RET^{V804M} under AD80 or vandetanib treatment (4h). **E)** Calculated K_m values of ATP binding to RET^{wt} or RET^{V804M}-mutant from three independent experiments are displayed. ***, $p < 0.001$.

Figure 4

A) Dose-response curves as assessed for AD80 against Ba/F3 cells expressing KIF5B-RET^{wt} (black) or KIF5B-RET^{I788N} (red) and CCDC6-RET^{wt} (black dashed) or CCDC6-

RET^{I788N} (red dashed). **B**) Column chart of mean GI₅₀-values + SD (from n=3) of KIF5B-RET^{wt} or KIF5B-RET^{I788N} Ba/F3 cells treated (72h) with AD80, cabozantinib (CAB), vandetanib (VAN) or ponatinib (PON). *p*-values are given as ”*”. **C**) Immunoblotting of KIF5B-RET^{wt} (left panel) or KIF5B-RET^{I788N} (right panel) and CCDC6-RET^{wt} or CCDC6-RET^{I788N} (lower panel) Ba/F3 treated (4h) with AD80 are displayed (4h). **D**) Immunoblotting of KIF5B-RET^{wt}, KIF5B-RET^{V804M} or KIF5B-RET^{I788N} Ba/F3 cells treated (4h) with ponatinib are shown. HSP90 is used as loading control. **E**) Optimized structure after extensive MD refinement followed by ALPB optimization. RET-wt/AD80 after 102 ns (side view). Distance from central phenyl’s center: 4.61 Å to Ile788-C(V804M).

Figure 5

A) RNA-Seq results of LC-2/AD cells treated (48h) with 100nM AD80 are shown. Genes contained within the core enrichments following GSEA against the hallmark gene sets with genes upregulated (KRAS up) or downregulated (KRAS down) by active KRAS are highlighted by red and green, respectively. The dashed line represents FDR-adjusted *q*-value= 0.05. **B**) Relevant genes from the top-50 genes with strongest and significant change in RNAseq after AD80 treatment (100nM/48h) are shown. **C**) The predicted number of down regulated phosphorylation sites for each kinase is shown. All kinases with ≥6 down regulated phosphorylation sites are shown in hierarchical order. Kinases associated with MAPK pathway signaling are highlighted in red. **D**) In immunoblotting assays RET signaling was monitored in LC-2/AD and TPC-1 cells, treated (48h) with either AD80 (0.1μM), trametinib (TRA) (0.1μM) or a combination of both inhibitors (combo). **E**) LC-2/AD^{ev} or LC-2/AD^{KRAS} G12V cells were treated (72h) with AD80. Results are shown as mean + SD (n=3). *p*-

values given as “*” are displayed. **F)** Immunoblotting of LC-2/AD^{ev} or LC-2/AD^{KRAS}^{G12V} cells under AD80 treatment (100nM/4h) is shown.

Figure 6

A) Immunoblotting of tumor tissue from CRISPR/Cas9 induced NIH-3T3^{KIF5B-RET} Xenografts was performed. Mice were treated (4h) with vehicle control, 12.5 or 25 mg/kg AD80, CAB or VAN and sacrificed. **B)** Median tumor volume was assessed using consecutive measurements of patient-derived xenograft (PDX) tumors driven by *CCDC6-RET*^{wt} or *CCDC6-RET*^{V804M} rearrangements under treatment with either 25 mg/kg AD80 (14d) or vehicle-control (14d). Treatment starts at day 0. **C)** Waterfall plot for each *CCDC6-RET*^{wt} fusion positive PDX depicting best response (14d) under AD80 or vehicle-control treatment is displayed. ***, $p < 0.001$. **D)** Waterfall plot for each *CCDC6-RET*^{V804M} positive PDX depicting best response (7d) under AD80 or vehicle-control treatment is displayed. ***, $p < 0.001$. **E)** Representative IHC stainings for H&E and Ki-67 of AD80 or vehicle control treated *CCDC6-RET*^{wt} derived PDX. Scale bar represents 100 μm . **F)** Ki-67 IHC staining and the plotted values are shown. ***, $p < 0.001$.

Figure 1

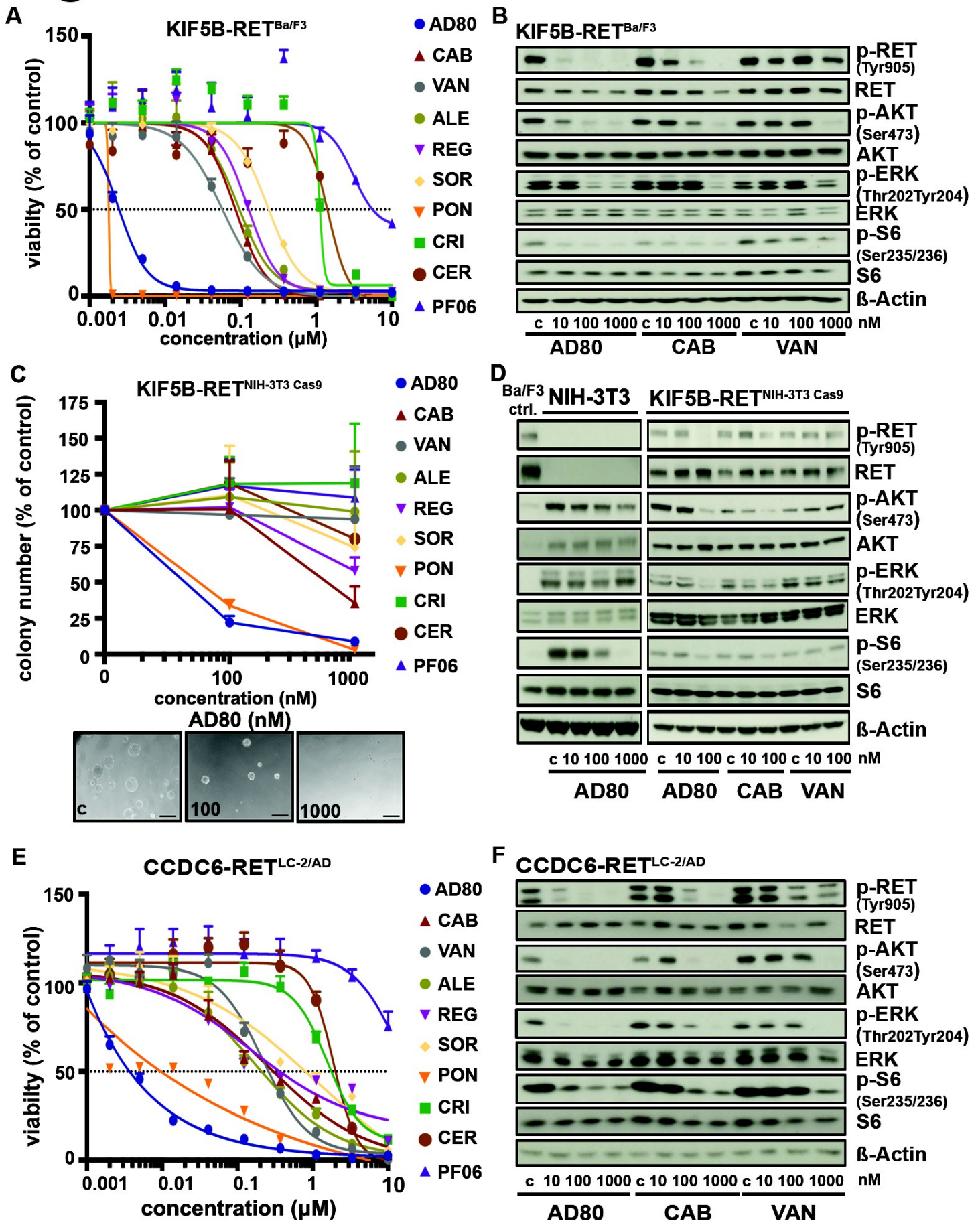
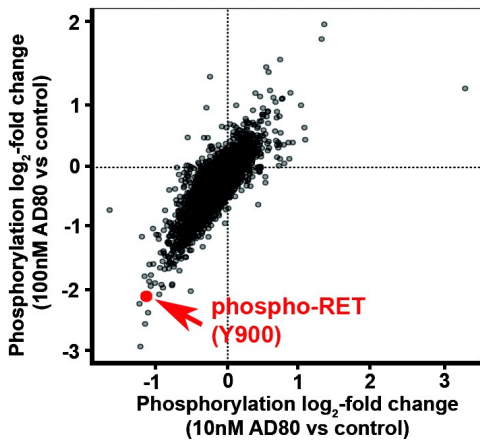


Figure 2

A



B

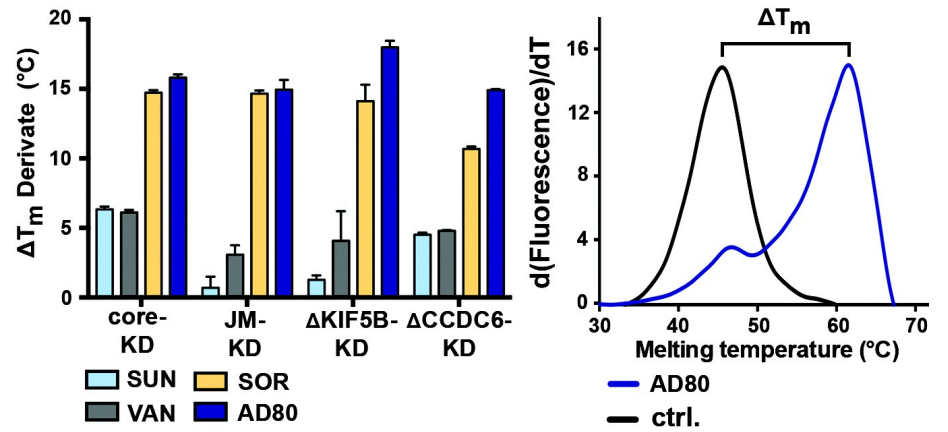
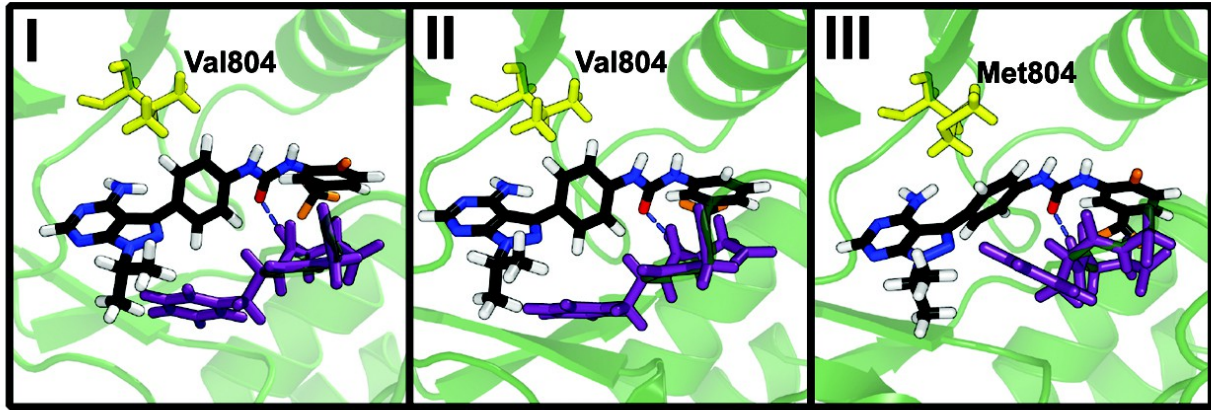
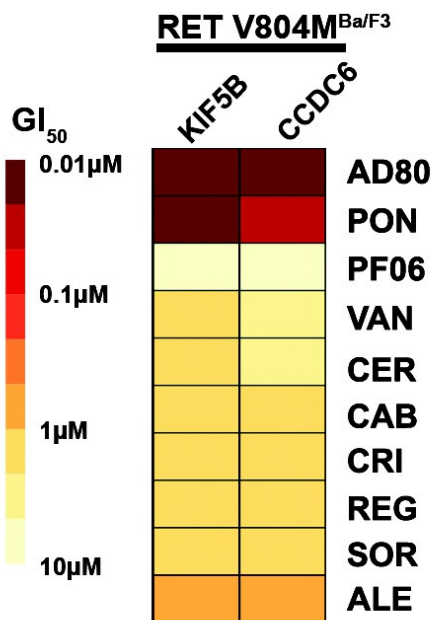


Figure 3

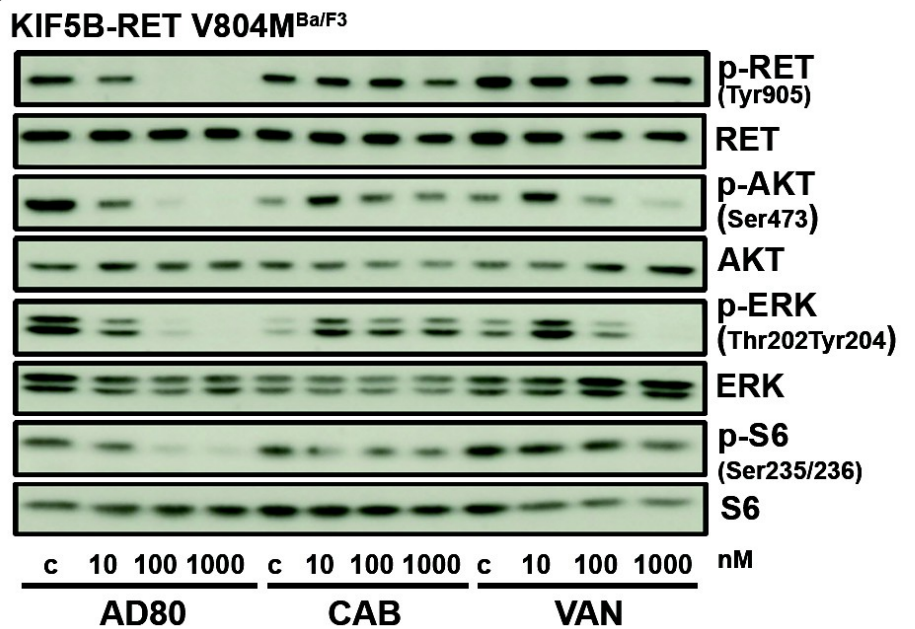
A



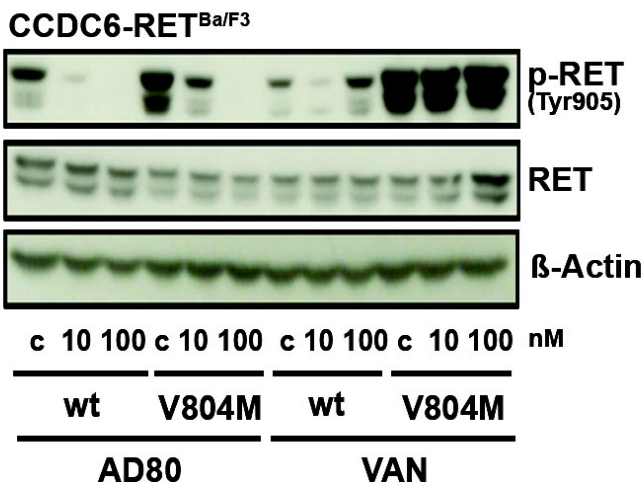
B



C



D



E

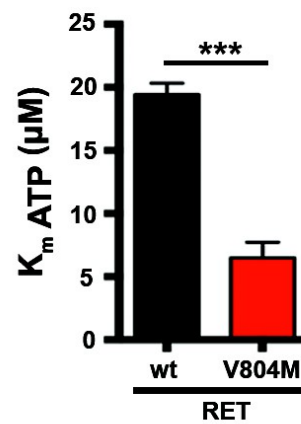


Figure 4

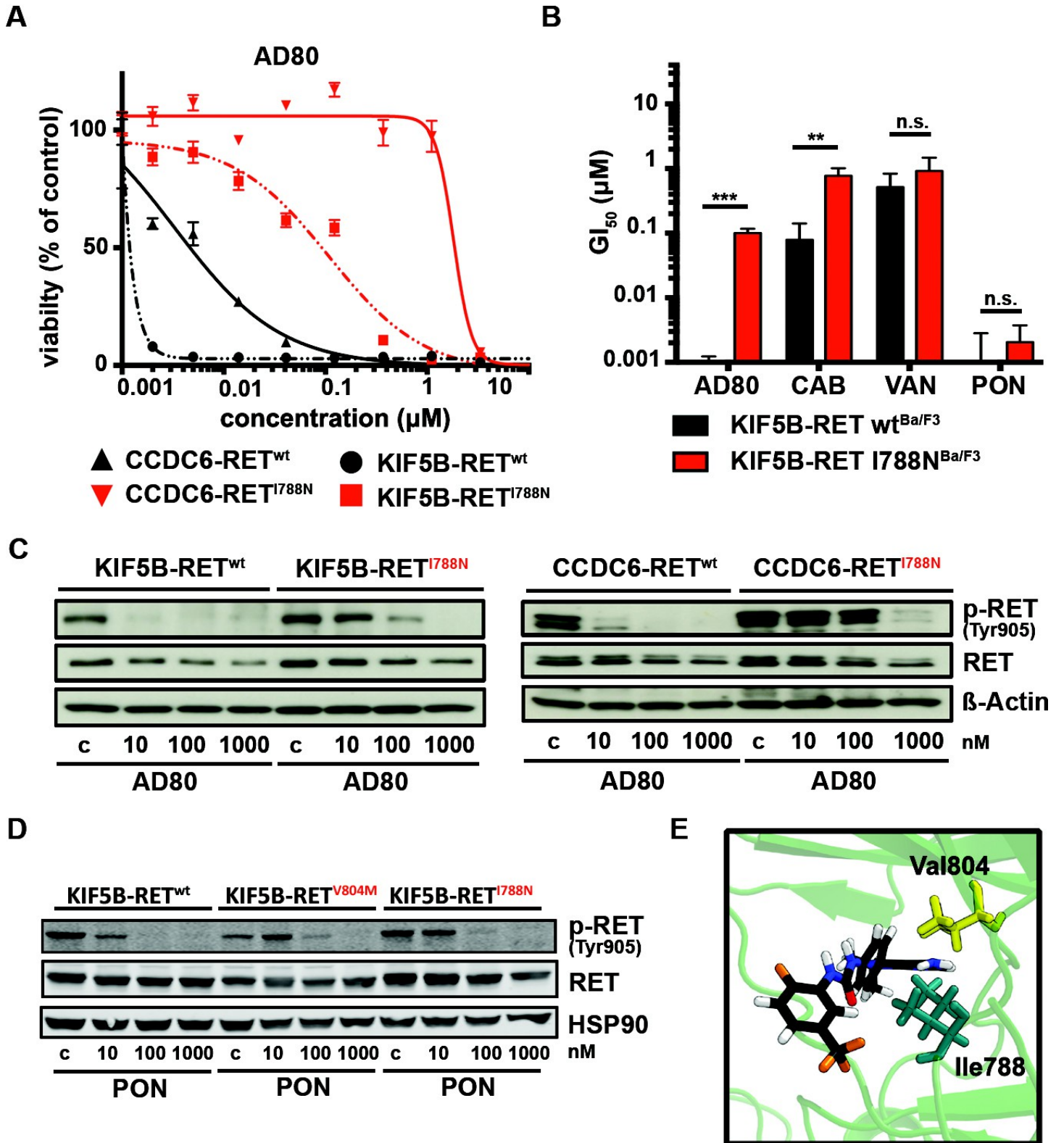


Figure 5

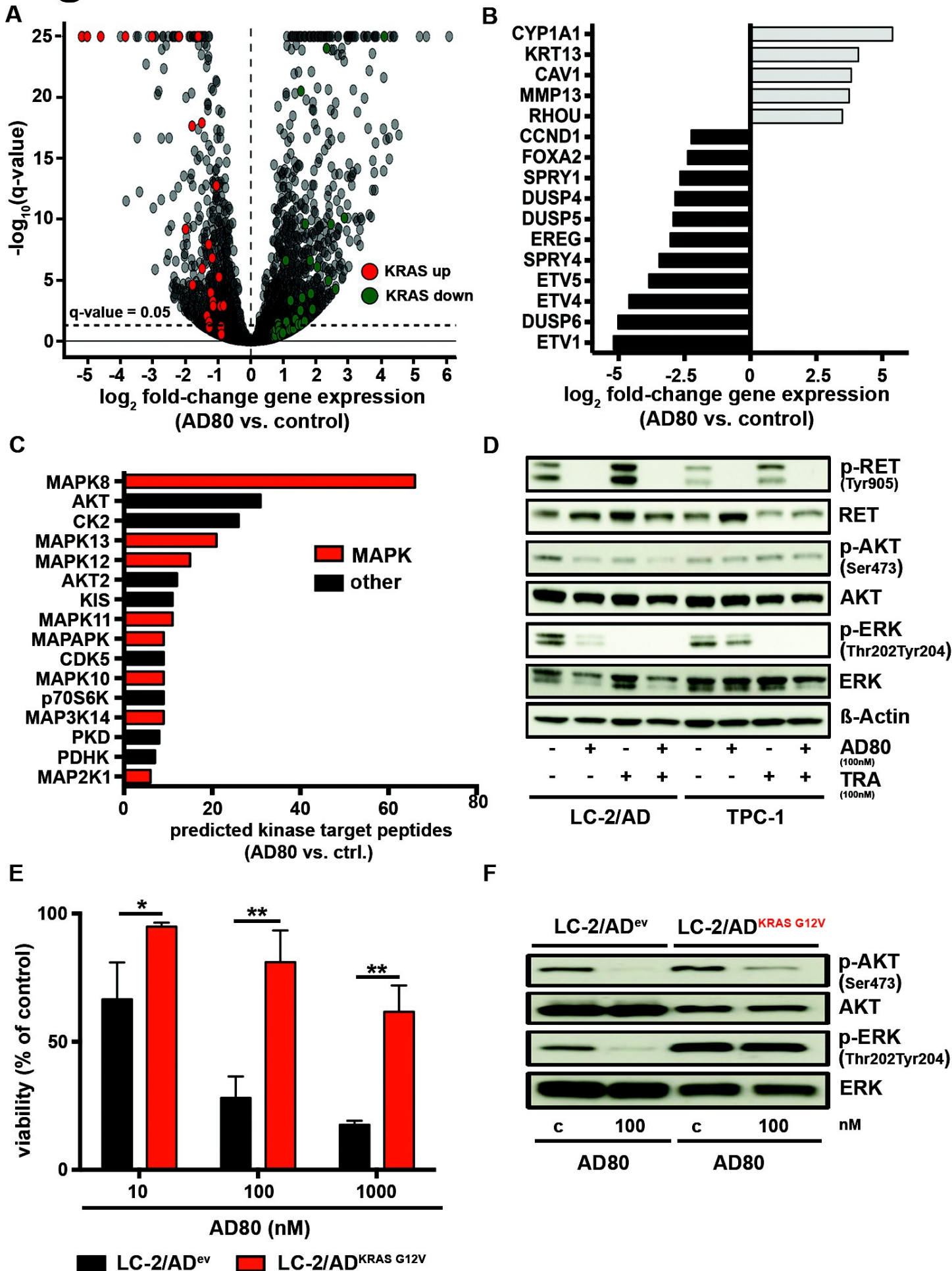
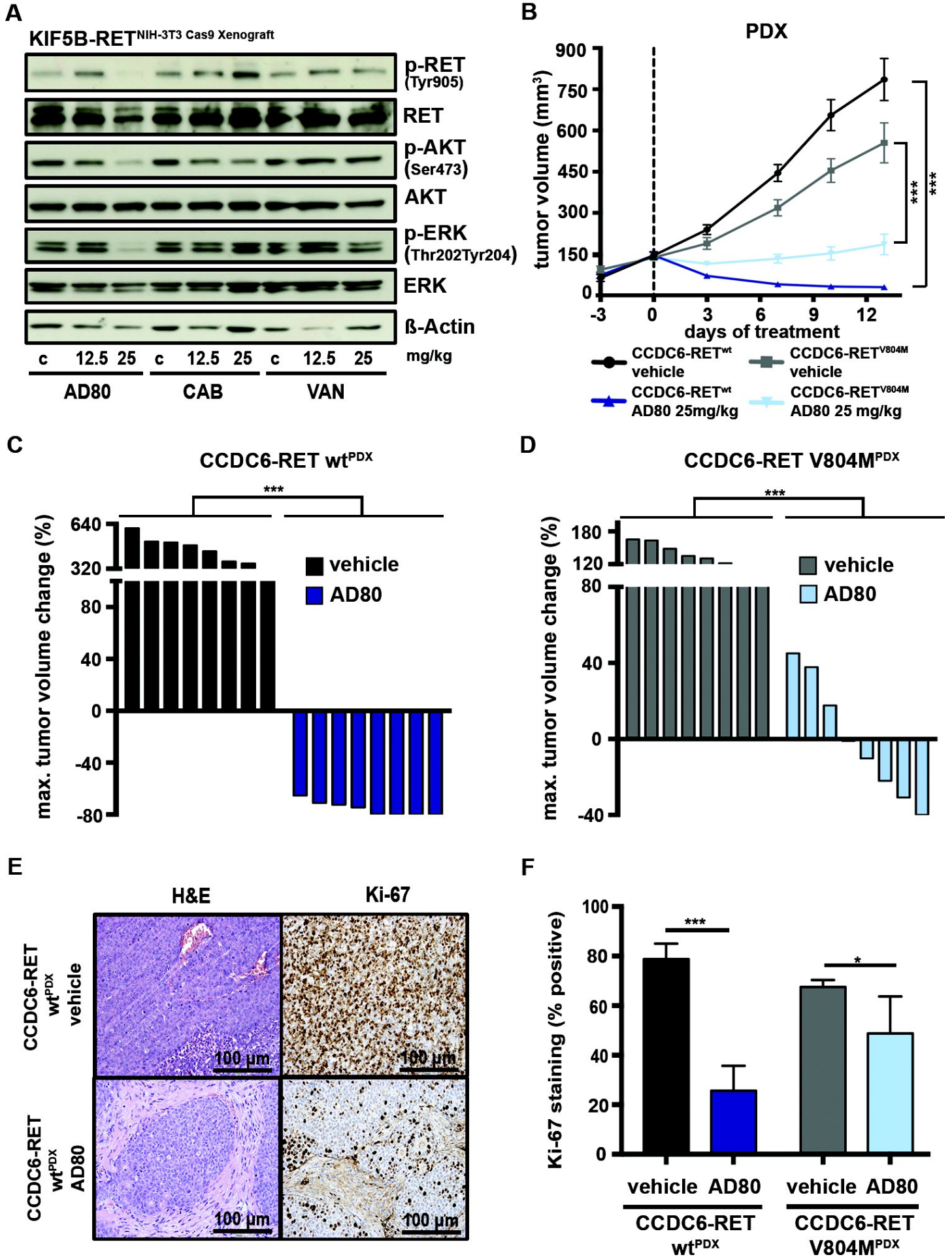


Figure 6



Supplementary Materials

Supplementary Materials and Methods

Methods

Fig. S1. Selective inhibition of signaling induced by rearranged RET.

Fig. S2. Characterization of the activity profile of AD80.

Fig. S3. Delineation of the cellular targets of AD80 using ligand screens and thermal shift experiments and comparison of type I and II RET kinase inhibitors.

Fig. S4. Root mean square deviations (RMSD) measurements of RET and AD80 or cabozantinib and optimized structures after extensive MD refinement followed by ALPB optimization.

Fig. S5. Inhibitory potential of AD80 derivatives and primary and secondary resistance against RET inhibition.

Fig. S6. Validation of PDX via FISH and *in vivo* effects induced by treatment with AD80.

Fig. S7. Limited clinical activity of currently available RET inhibitors and validation of a small cohort of patients with *RET*-rearrangements.

Table S1. IC₅₀ values of AD80, cabozantinib and vandetanib for phospho-RET levels in Ba/F3 cells expressing wild type or V804M *KIF5B-RET*.

Table S2. GI₅₀ values of the panel of patient-derived cell lines.

Table S3. Tabulated derivative melting temperatures (T_m) and differences in melting temperature (ΔT_m) values.

Table S4. *In vitro* kinase assay of RET wt, V804M and V804L mutants with different inhibitors.

Table S5. Experimental setup for saturated mutagenesis screening.

Table S6. Clinical response rates to currently available anti-RET drugs and clinical information of patients used in retrospective analysis.

References (41-64)

Methods

Study population

All patients consented to testing, therapy and registration of data for future publication. *RET* FISH testing was performed by experienced pathologists (RB, JD) as described before (33). All tumors were negative for coexisting mutations of *EGFR*, *ALK*, *ROS1*, *HER2* or *BRAF*. Rebiopsies of P1 and P2 were sequenced using hybrid capture-based next-generation sequencing (NEO, New Oncology AG). Available RET inhibitors were given off-label (sunitinib, vandetanib) or compassionate use (cabozantinib) in accordance with local regulations. Follow up was performed by PET or CT scans in intervals of 2-4 weeks, and interpreted by radiologists. Response rates were measured according to RECIST 1.1 criteria.

Antibodies used for immunoblot

The following antibodies were obtained from Cell Signaling: p-AKT Ser473 (Catalog No. #9271), p-ERK1/2 Thr202/Tyr204 (Catalog No. #4370), p-S6 Ser235/236 (Catalog No. #4858), p-RET Tyr905 (Catalog No. #3221), AKT (Catalog No. #9272), ERK 1/2 (Catalog No. #9102), S6 (Catalog No. #2217), RET (Catalog No. #3220). HSP90 (#SPA-835) was purchased from Enzo.

Antibodies were diluted in TBST containing 5% milk (Carl Roth) and incubated at 4°C overnight on a shaker. Actin as a loading control was detected via an actin-horseradish peroxidase (HRP) antibody (Santa Cruz Biotechnology (Catalog No.

#sc47778). Detection of proteins was performed via HRP-conjugated anti-mouse anti-rabbit antibodies (Millipore) via enhanced chemiluminescence (ECL) reagent (GE Healthcare) or via near infrared fluorescent dye coupled antibodies (LI-COR Biosciences). Due to overlapping molecular weights not all proteins were detected at the same membrane per displayed figure panel.

Cell culture

LC-2/AD cells were obtained from Sigma Aldrich. TPC-1 cell line was a kind gift from Dr. William Pao. Ba/F3 murine pro-B-cell line was a kind gift from Nikolas von Bubnoff. NIH-3T3 murine fibroblast cell line was purchased from DSMZ. All cell lines were grown in a humidified incubator at 37°C and 5% CO₂ in the corresponding recommended media supplemented with antibiotics and fetal calf serum.

Viability and Colony formation assays

3,000 (adherent) or 10,000 cells (suspension) for viability assays in 96-well plates and 10,000 cells for colony formation assays in 12-well plates were used and analyzed as previously described (38). GI₅₀-values were determined with GraphPad Prism 6.0h.

Molecular cloning and viral transduction

Full length *KIF5B-RET* and *CCDC6-RET* were cloned in the retroviral vector pBabe-puro (Addgene #1764) via Gibson assembly (NEB). KRAS-G12V was cloned via Gibson Assembly into the pLenti6 backbone (Thermo Scientific™). Site-directed mutagenesis was performed using Q5® polymerase (NEB). Mutations and analysis of complete inserts were confirmed via Sanger sequencing at the Cologne Center for Genomics. pBabe and pLenti vectors were co-transfected with corresponding helper

plasmids with TransIT-LT1 (Mirus) using standard procedures in HEK293T cells. After several passages we observed a decrease in fitness of *KRAS*^{G12V} transduced LC-2/AD cells.

Undirected mutagenesis

The cDNAs of *CCDC6-RET* and *KIF5B-RET* were cloned into the pBabe puro backbone. Undirected mutagenesis was performed via *E. coli* XL1-Red (Stratagene) bacteria cells for 24/48/72h as previously described (23, 24). After viral transductions in Ba/F3 cells, cells were challenged with 200nM AD80. After outgrowth, genomic DNA was isolated and sequenced using capture-based sequencing (CAGE) at NEO oncology.

FISH

Tumor specimens were stained with KIF5B and RET break-apart FISH probes were purchased from Zytovision. Per case 100 carcinoma cells were analyzed for rearrangements. Positivity was defined as $\geq 20\%$ of cells showing aberrant patterns indicative of KIF5B- / RET-rearrangements: i) One break-apart (isolated red and isolated green signal) and one or more fusion signals ii) One or more isolated green signals and one or more fusion signals.

Phosphoproteomal analysis

Materials

If not mentioned otherwise chemicals were purchased from Sigma Aldrich in the highest purity available. ULC-MS acetonitrile (ACN), formic acid (FA) and trifluoroacetic acid (TFA) were from Biosolve BV. Ultra-pure water was obtained from an ELGA Purelab flex water purification system (ELGA Labwater). C18 solid

phase extraction was conducted using SPEC C18-AR cartridges (Agilent Technologies).

Proteomics sample preparation

Protein concentrations of cell lysates were determined by a Pierce bicinchoninic-acid assay kit (Thermo Fisher Scientific) according to the manufacturer's instructions. To degrade DNA samples were treated with 25U Benzonase[®] (Merck) in the presence of 2mM MgCl₂ and incubated at 37°C for 30min. Cysteins were reduced with 10mM dithiothreitol (DTT) for 30min at 56°C. Afterwards, free cysteines were alkylated with 30mM iodoacetamide (IAA) for 30min at RT in the dark. Excess IAA was quenched by addition of 10mM DTT for 15min. Proteolytic digestion was conducted using a modified filter aided sample preparation procedure (41): Per sample 150µg of protein was diluted with freshly prepared 8M urea, 100mM TRIS buffer (pH 8.5) to a final concentration of 7mM SDS and 6.4M urea (42). Samples were passed over 30kDa Pall Nanosep Omega molecular weight cut off centrifuge filters (VWR International) by centrifugation for 25min at 13,500g, followed by three washing steps with 8M Urea, 100mM TRIS, pH 8.5 and another three steps with 50mM triethylammonium bicarbonate buffer (TEAB, pH 8.5). Trypsin (sequencing grade modified, Promega) was added in a 1:25 ratio in 150µL of 50mM TEAB, 0.2M guanidine hydrochloride and 2mM CaCl₂ and samples were incubated at 37°C for 14h. Generated peptide mixtures were collected from the filters by centrifugation, followed by two washing steps with 50µL of 50mM TEAB and H₂O, respectively. Samples were acidified to pH ~2.0 with TFA and 1µg per sample was used to control digest efficiency and reproducibility as described elsewhere (43).

TMT-labelling, multiplexing and sample cleanup:

A mixed sample containing 150µg of peptide was generated using equal amounts of the 9 different conditions. Afterwards, 150µg per sample were labeled with TMT 10-plex reagents (Thermo Fischer GmbH) according to the manufacturer's protocol (controls: 126, 127N, 127C; 10nM AD80: 128N, 128C, 129N; 100nM AD80: 129C, 130N, 130C; mixed sample: 131). After labeling and quenching with 5% hydroxylamine, samples were multiplexed, dried under vacuum and reconstituted in 300µL of 0.1% TFA. Next, samples were desalted on a 50mg SPE cartridge and an aliquot corresponding to 40µg of peptides was taken for global proteome analysis (see below).

Phosphopeptide enrichment and fractionation

Phosphopeptides were enriched by TiO₂ as described by Engholm-Keller et al. with slight modifications (44). Briefly, the multiplexed sample was incubated in 5% TFA, 80% ACN, 1M glycolic acid together with an excess of TiO₂ beads for 3 times (beads to peptide ratios were 1:6, 1:3 and 1:1.5), and peptides were eluted from the beads with 1.12% NH₄OH. A second sequence of incubations with the same amounts of fresh TiO₂ beads in 70% ACN, 2% TFA was performed to achieve maximum enrichment specificity. The phosphopeptide-enriched sample was desalted using Oligo R3 (Applied Biosystems) (39). Phosphopeptides were reconstituted in HILIC loading buffer (98% ACN, 0.1% TFA) and directly fractionated by hydrophilic interaction liquid chromatography (HILIC) on an Ultimate 3000 RSLCnano system (Thermo Fisher Scientific) equipped with a self-packed 250µM x 15cm column filled with TSK GelAmide 80 material (3µM, 100Å, Tosoh Bioscience GmbH, Stuttgart, Germany). A 37min gradient from 10-35% of 0.1% TFA was used to obtain a total of 16 fractions for LC-MS/MS analysis.

High-pH reversed phase fractionation:

For the global proteome analysis, 40 μ g of labeled peptides were fractionated by high pH RP chromatography using an UltiMate 3000 HPLC (Thermo Fisher Scientific). The peptide sample was redissolved in 10mM ammonium formate (pH 8.0, adjusted with FA) and separated on a BioBasic C18 column (500 μ M x 15cm, 5 μ M, 300 \AA , Thermo Fisher Scientific) with a flowrate of 12.5 μ L/min at 30 $^{\circ}$ C using a gradient from 3-50% of 10mM ammonium formate, 84% ACN, pH 8.0 in 70min. Fractions were collected between 10-80min in concatenation mode (1min intervals) to yield a total of 20 fractions. Fractions were dried under vacuum and reconstituted in 32 μ L of 0.1% TFA, 50% per fraction were subjected to LC-MS/MS analysis.

Nano LC-MS/MS analysis

Nano LC-MS/MS was conducted on an Ultimate 3000 RSLCnano system equipped with Acclaim PepMap C18 columns (precolumn: 100 μ M x 2cm, 5 μ M, 100 \AA ; main column: 75 μ m x 50cm, 3 μ M, 100 \AA ; both Thermo Scientific). Samples were reconstituted in 0.1% TFA and trapped on the precolumn for 10min at a flowrate of 20 μ L/min 0.1% TFA. Peptides were separated using a binary gradient and solvents A (0.1% FA) and B (84% ACN, 0.1% FA) ranging from 3-35% B in either 60min (phospho) or 90min (global and phospho). The HPLC was online connected to a Q-Exactive HF mass spectrometer (Thermo Fisher Scientific) via a nano-ESI interface in positive ion mode and samples were analyzed in data dependent acquisition mode (DDA). Survey scans were acquired with a resolution of 60,000, an AGC target value of 1×10^6 and a maximum injection time of 120ms. The top 15 most intense signals with charge states 2-5 were subjected to MS/MS using dynamic exclusion of 30s, an isolation width of 0.8 m/z , an NCE of 33%, a resolution of 60,000, an AGC target value of 2×10^5 and a maximum injection time of 200ms, with the first mass set to

100 m/z . To compensate for a higher complexity of the global proteome fractions, the isolation width was reduced to 0.4 m/z to reduce the potential precursor co-isolation.

Data analysis:

All raw files were searched against the human Swiss-Prot database (www.Uniprot.org; April 2016, 20,207 target sequences) using Mascot v 2.4.1 (Matrix Science) and the Proteome Discoverer 1.4 software package (Thermo Fisher Scientific). Search settings were as follows. Trypsin was used as enzyme with a maximum of 2 missed cleavage sites. Mass tolerances were 10ppm for precursors and 0.02Da for fragment ions. TMT 10-plex (+229.163Da on Lys and N-termini) and carbamidomethylation of Cys (+ 57.021Da) were set as static modifications. Phosphorylation of Ser/Thr/Tyr (+ 79.966Da) and oxidation of Met (+ 15.995Da) were set as dynamic modifications. Phosphorylation site confidence was determined using phosphoRS 3.1 and false discovery rate assessment was performed using Percolator (45, 46). For the phosphopeptide data analysis, only unique peptide-spectrum-matches (PSMs) with high confidence (< 1% FDR), a search engine rank of 1 and a minimum phosphoRS site localization probability of 0.9 for all sites were considered. For the global proteome only proteins quantified with at least 2 unique high confidence peptides were considered. Sorting and evaluation of the exported data as well as calculations were done in Microsoft Excel 2013.

Global proteome: As Proteome Discoverer only provided 9 ratios for the 10 samples, an artificial 126/126 ratio was created and set to 1.0 per protein. For each channel a median over all protein log₂-ratios was calculated (MD1₁₂₆₋₁₃₁). Next, the median over all ten MD1 values was determined (MD2) to define normalization values (NV) per channel and these MD2 were subtracted from the individual MD1 values. This

normalization was performed to compensate for individual systematic errors (i.e. unequal sample amounts derived from pipetting errors or inaccurate BCA results) and to obtain normalized log₂-ratios (NR) per protein (126/126, 127/126, ..., 131/126). Next, for each protein the median over all ten NRs was subtracted from the individual NRs to obtain scaled normalized abundance values (NAV) for all proteins and channels after retransformation to decadic values.

Per protein NAVs of the three biological replicates were summed and used to obtain protein ratios between different conditions (e.g for 10nM AD80 vs. control: sum(128N,128C,129N)/sum(126,127N,127C)). Additionally, a Student's t-test (two sided, homoscedastic) was applied between the respective triplicate groups of NAVs for each comparison.

The global median (GM) and the global standard deviation (GSD) over all log₂ protein ratios were then calculated for each comparison and values greater than GM + 3*GSD or smaller than GM - 3*GSD were considered as potentially regulated, if the corresponding p-value was ≤ 0.05 .

Phosphoproteome: The NVs, GMs and GSDs from the global proteome were used to process the phosphoproteomics data. First, for each TMT channel the areas of all PSMswere divided by their respective NVs to yield normalized areas (NAs). The NAs for each PSM were then scaled by dividing them by the median over all ten NAs to yield the normalized abundance values of phosphopeptide-PSMs (p-NAV_s). The p-NAV_s of multiple PSMs corresponding to a specific phosphopeptide (same sequence, same phosphorylation site(s)) were averaged for each channel to obtain the averaged normalized abundance values of phosphopeptides (p-NAV_{avr}). The p-NAV_{avr}s were used to obtain ratios between biological conditions and corresponding p-values were

determined as above. The ratios were subsequently log₂-transformed. A phosphopeptide was considered as potentially regulated between conditions, if (i) the log₂ ratio was greater than GM + 3*GSD or smaller than GM - 3*GSD; (ii) the corresponding p-value between was ≤ 0.05 , (iii) the corresponding protein was not regulated in the global proteome data to ensure, that an apparent phosphorylation site regulation is not rather a change of expression during the 4h stimulation experiment.

For computational prediction of kinases with altered activity from the differentially regulated phosphorylation sites observed in the phosphoproteome we used the group based kinase prediction algorithm (GPS) version 2.1.2 by Xue et al. (47). The FASTA formatted sequences of proteins with regulated phosphorylation sites were provided to GPS (high confidence threshold) for kinase prediction. Per site only the highest ranking high confidence kinase prediction was considered and the altered phosphorylation sites per kinase were quantified.

Protein Thermal Shift assay

Constructs

Constructs were prepared as described previously (17). In addition, Δ CCDC6-KD (residues 54 to 101 fused to RET 713 to 1012) and Δ KIF5B-KD (residues 544 to 757 fused to RET 713 to 1012) both including the D874N mutation to generate kinase dead constructs were ordered from Genart (Life Technologies). Baculovirus production was carried out in the same manner as previously described (17).

Protein Production

SF21 cells were grown in SF-900 III SFX media with 10µg/ml gentamycin in shaker flasks at 27°C for protein production. Viral infections were performed on high density cells (5×10^6 cells/ml) supplemented with 1% glucose (Sigma), 6.64g/L yeastolate (Difco) and lactalbumin (Sigma). Cells were harvested 72 hours post-infection, resuspended in lysis buffer (20mM Tris pH 8.0, 150mM NaCl, 1mM DTT, 10mM Benzamidine, 0.2mM AEBSF), lysed by sonication and purified by incubation with glutathione-Sepharose 4B beads (Amersham Biosciences). Purified proteins were either dephosphorylated using 10 units of CIP (NEB) and 10mM MgCl₂, or the core-KD and JM-KD were phosphorylated with 2.5mM ATP and 10mM MgCl₂. The immobilised ΔKIF5B-KD and ΔCCDC6-KD proteins were phosphorylated using purified solubilised JM-KD, 2.5mM ATP and 10mM MgCl₂. Dephosphorylation and phosphorylation steps were all carried out for either 2 hours at RT or overnight at 4°C. Proteins were subsequently washed and cleaved from resin using a GST-linked 3C protease. Purified ΔKIF5B-KD and ΔCCDC6-KD proteins were additionally purified by size exclusion chromatography on a Superdex 200 column and all proteins were concentrated in HEPES buffer (20mM HEPES pH 8.0, 150mM NaCl and 1mM DTT) to 0.1mg/ml.

Protein Thermal Shift

Control or drug treatments were incubated with DMSO or indicated drug at a final concentration of 1 µM both to a final DMSO concentration of 1% and incubated for up to 30 minutes on ice. Sypro-Orange dye (Life Technologies) was subsequently added and incubated. Quadruplicates of each sample per experiment were set up in MicroAmp Fast Optical 96-Well Reaction Plates (Applied Biosystems) and plates were sealed and run in a 7500 Fast RT PCR machine (Applied Biosystems) with a

temperature range of 25 – 90°C. Data was analysed using the Protein Thermal Shift Software v1.2 (Applied Biosystems). Derivative melt curve plots were used for final data analysis to generate the proteins melting point (T_m) and the difference in melting temperatures (ΔT_m). Results were then averaged across experiments and SEM values were calculated.

Computational binding mode modeling

Similar to the initial steps in (19), we selected VEGFR (pdb code 2OH4 (18)) as template for modeling the relevant part of the wt RET protein due to the large sequence identity and availability of the DFG-*out* structure. Filling of sequence gaps and structure preparation was done using Modeller 9.14 (48). An initial estimate of the wt binding mode for AD80 was created by superimposing the chemically equivalent part of AD80 with the GIG ligand as provided in the template structure file. Because to the best of our knowledge no cabozantinib structure bound to a kinase domain is deposited in the PDB we generated an initial binding pose of cabozantinib to RET (wt) in a similar manner based on the final RET/AD80 model (see below). For that purpose we took the chemically equivalent part of the XL880 ligand bound to the c-Met kinase (PDB code 3LQ8) and superimposed it onto the RET(wt)/AD80 complex followed by converting XL880 to cabozantinib. Two reasonable conformers of the quinoline ring system were initially created and the energetically favorable geometry was selected after energy minimization in an implicit water model environment (ALPB) (49). While Amber ff99sb (50) was chosen as the protein force field, we followed closely the preparation procedure outlined recently for the (assumed neutral) ligand models (51).

All-atom molecular dynamics (MD) simulations for the RET complexes were performed by immersing them in 25428 (AD80) and 27987 (cabozantinib) TIP3P (52) water molecules after neutralizing with 8 chloride counterions employing NAMD 2.10 (53) at a temperature of 298.15K using a time step of 2 fs. MD runs were conducted in a sequence of steps to ensure stability. An initial 4 ns were performed in the canonical ensemble applying harmonic restraints on protein C^α atoms and the ligand, followed by restrained 4ns in the isothermal-isobaric ensemble at 1 bar pressure to relax the volume. After lifting all restraints, additional 92 ns were simulated in the isothermal-isobaric ensemble. We checked the stability of these completely free systems by monitoring root mean square deviations (RMSD, **Fig. S4A**) from the initial structure, indicating sufficient stability. The resulting snapshot was optimized under ALPB conditions in Amber 12,(50) followed by point mutation by Modeller (54) to generate the V804M mutant. This structure was refined using a similar simulation protocol as for the wt, followed again by ALPB optimization. The initial structure for the RET(wt)/cabozantinib model was built based on the last frame of the RET(wt)/AD80 simulation, followed by further 112ns of isothermal-isobaric. The resulting snapshot was then treated in the same way as the RET/AD80 complexes.

The end point of the RET/AD80 simulation was used as starting point for thermodynamic integration (TI) MD simulations which were performed with pmemd in Amber 12 (50). This was done in order to estimate the binding free energy difference between AD80 and AD57 in the presumed DFG-*out* bound protein conformation, which differ only by a single atom (F in AD80 is alchemically transformed to H in AD57). Using MD settings as before, 11 consecutive coupling parameter (λ) windows ($\delta\lambda = 0.1$, 10 ns within each window) were simulated,

dropping the initial 3 ns per window and using the remaining 7 ns for averaging in the isothermal-isobaric ensemble. To assure correct physics, the transformed hydrogen atom of AD57 was excluded from the bond constraint algorithm.

In order to (roughly) estimate the binding free energy difference for AD80 bound to wt RET and to the V804M mutant, we performed single-state 3D RISM calculations on the final optimized structures, we essentially follow the methodology described in (40, 55-57). Briefly, the optimized complex partners were separated, keeping their internal geometries fixed. Independent 3D RISM calculations were performed in an aqueous environment (cubic grids of 340^3 points with 0.3 Å spacing, second order partial series expansion closure, 298.15K, TIP3P water model parameters and conditions as in Ref. (57)) in order to yield the solvation free energies of the complex and the individual partners (40, 57). Applying this procedure for 10 ALPB-optimized snapshots taken every 1 ns from the last available frames of RET^{wt}/AD80, RET^{wt}/AD57, and RET^{V804M}/AD80 simulations and adding the direct interaction energy of the complex partners yields a “per snapshot” estimate of the binding free energy. These values enter a discrete canonical partition function expression by Boltzmann weighting, from which the final estimates of the ensemble binding free energy difference were computed. These can be compared to experimental values via $-RT \ln IC_{50}(\text{educt})/IC_{50}(\text{product})$, RT being the product of molar gas constant and temperature.

RNA sequencing

RNA was isolated from duplicates of LC-2/AD cells following 48h treatment with 100 nM AD80 or DMSO controls using the RNeasy Kit (Qiagen) following the manufacturers' protocols. RNA quality and integrity was verified using a TapeStation

(Agilent Technologies). Strand specific libraries were prepared using the TruSeq® Stranded mRNA sample preparation Kit. Library preparation started with 1 µg total RNA. After poly-A selection (using poly-T oligo-attached magnetic beads), mRNA was purified and fragmented using divalent cations under elevated temperature. The RNA fragments underwent reverse transcription using random primers. This is followed by second strand cDNA synthesis with DNA Polymerase I and RNase H. After end repair and A-tailing, indexing adapters were ligated. After purification, 10ul template was used for amplification (14 PCR cycles) to create the final cDNA libraries. After library validation and quantification (Agilent 2100 Bioanalyzer), equimolar amounts of library were pooled. The pool was quantified by using the Peqlab KAPA Library Quantification Kit and the Applied Biosystems 7900HT Sequence Detection System. The pool was sequenced by using a HiSeq® 3000/4000 PE Cluster Kit and a HiSeq® 3000/4000 SBS Kit on an Illumina HiSeq 4000 sequencer with a paired- end (76x7x76 cycles) protocol. Reads were mapped to the hg19 reference genome with TopHat and to genomic features according to the Illumina iGenomes hg19 gene annotation with the GenomicsFeatures v1.22.13 package (58, 59). Differential expression analysis was performed using DESeq2 v1.10.1 with standard parameters (except for independentFiltering=F) (60). q-values were calculated from raw p-values by Benjamini-Hochberg FDR adjustment for multiple testing.

Gene set enrichment analysis

Genes were ranked based on the log fold change divided by the standard error of the log fold change to incorporate both direction and significance of treatment effects. To analyze effects on MAPK signaling ranked lists were input into the GSEA Java

application pre-ranked tool and queried against gene sets including genes down-regulated (HALLMARK_KRAS_SIGNALING_DN) or genes up-regulated (HALLMARK_KRAS_SIGNALING_UP) by KRAS activation as defined by the Hallmark gene sets (27, 61, 62). Genes contributing most to the enrichment score (core enrichment) were recorded and visualized.

Kinase selectivity score

To quantify the cytotoxic selectivity of compounds we calculated a compound's cell line selectivity similar to the kinase selectivity score approaches proposed by Davis et al. and Karaman et al. (63, 64). To this end we defined the genotype of the most sensitive cell line per compound as the main target and termed the corresponding concentration the primary GI₅₀. In all cases the altered gene of the most sensitive cell line was among the intended targets of respective inhibitors. Similar to the concept of a 'therapeutic window' we then calculated for each compound the ratios of the other cell lines' GI₅₀'s to the primary GI₅₀ to estimate which fold-increase of concentration relative to the primary GI₅₀ is possible before growth of cell lines with other genotypes is impaired. This analysis showed that the GI₅₀ concentrations of compounds with known high selectivity such as BGJ398 and ceritinib could be increased by 94-fold and 230-fold, respectively, before viability of a second cell line was decreased by 50% (**Fig. S2A,B**). In contrast, for the known multi-kinase inhibitors vandetanib and cabozantinib effects across other cell lines were already present at much lower ratios (**Fig. S2A,B**).

Clustering of cell lines based on drug sensitivity

For visualization cell lines were clustered based on GI₅₀ values and depicted as a heatmap indicating compound sensitivities and genotypes.

Statistical analyses

All statistical analyses were performed using Microsoft Excel 2011 or GraphPad Prism 6.0h for Mac or R (<https://www.r-project.org/>). *P*-values were assessed using Student's *t*-test unless specified otherwise. Significance is marked with * *p*-value ≤ 0.05, ** *p*-value ≤ 0.01 or *** *p*-value ≤ 0.001.

Supplemental Figures

Supplementary Figure 1

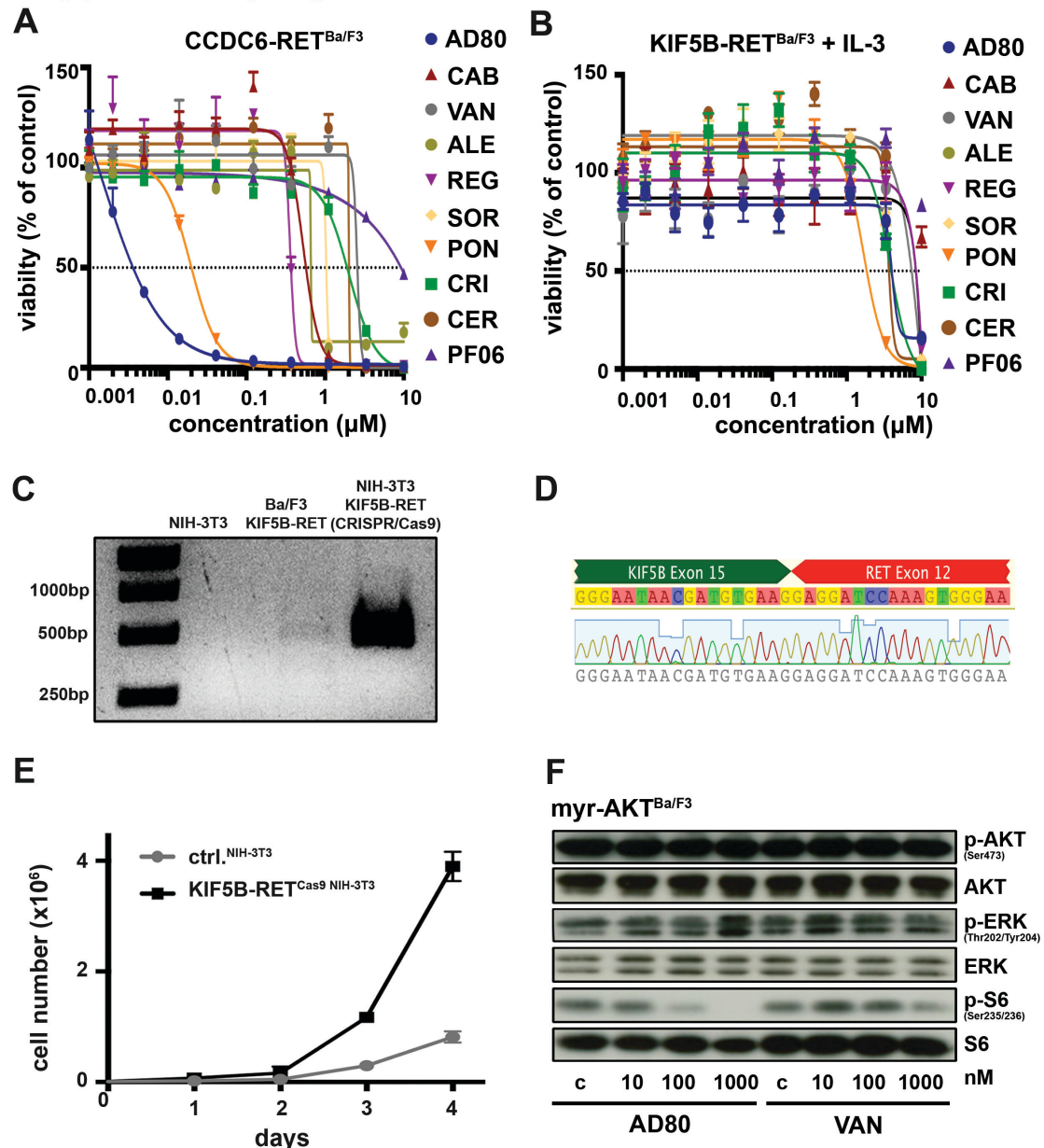


Fig. S1. Selective inhibition of signaling induced by rearranged RET.

A) Ba/F3 cells expressing *CCDC6-RET^{wt}* were treated (72h) at increasing doses of AD80, PF06463922 (PF06), regorafenib (REG), crizotinib (CRI), sorafenib (SOR), ponatinib (PON), vandetanib (VAN), ceritinib (CER) or cabozantinib (CAB) and the corresponding viability curves were assessed. **B)** The same setting was used in Ba/F3 cells expressing *KIF5B-RET^{wt}* in the presence of IL-3 is shown. **C)** The PCR product of the cDNA fusion transcript from NIH-3T3 cells with CRISPR/Cas9 induced *KIF5B-RET* fusion is displayed. Parental NIH-3T3 cells and Ba/F3 cells expressing *KIF5B-RET* serve as control. **D)** Chromatogram from Sanger sequencing of NIH-3T3 cells with CRISPR/Cas9 induced *KIF5B-RET* fusion. **E)** Median cell number growth (up to 96h) from consecutive measurements \pm SD (from n=3) comparing NIH-3T3 cells and NIH-3T3 cells with CRISPR/Cas9 induced *KIF5B-RET* fusion. **F)**

Immunoblot of Ba/F3 cells expressing *myr-AKT* under AD80 or vandetanib (VAN) treatment (4h).

Supplementary Figure 2

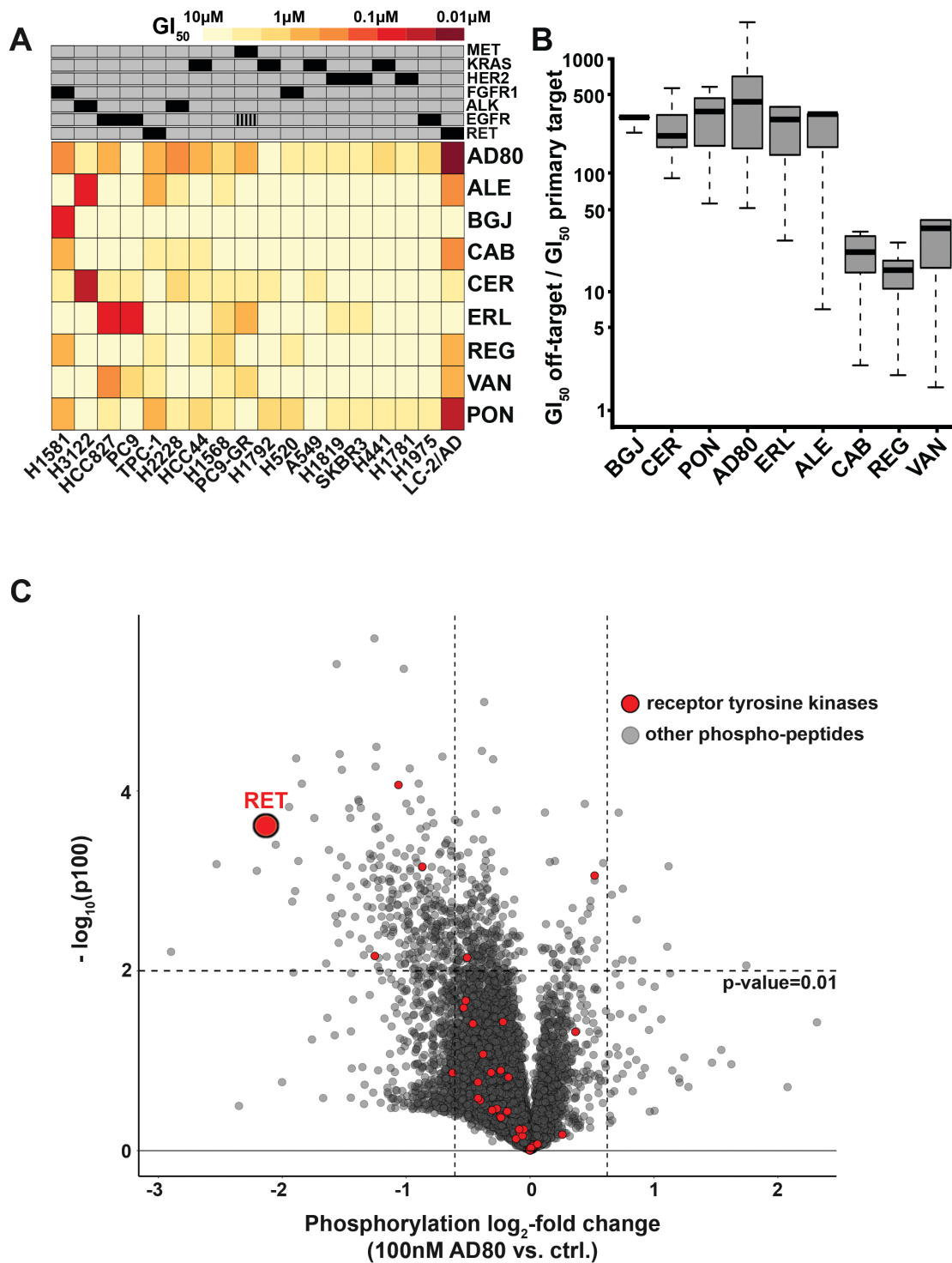


Fig. S2. Characterization of the activity profile of AD80.

A) Heat map of viability screening results from a panel of patient-derived cancer cell lines treated (72h) with AD80, alectinib (ALE), BGJ398 (BGJ), cabozantinib (CAB), ceritinib (CER), erlotinib (ERL), regorafenib (REG), vandetanib (VAN) or ponatinib (PON). Results are shown as average GI₅₀ values (n=3). The main oncogenic drivers are shown in the upper panel: *EGFR* mutant/ *MET* amplification (PC9-GR), *KRAS* mutant (H441; H1792; A549; HCC44), *HER2* overexpression (SKBR3; H1819), *Her2*

mutant (H1781), FGFR1 amplification (H1581; H520), *EML4-ALK* fusion (H3122; H2228), EGFR mutant (H1975; PC9; HCC827), *RET* fusion (LC-2/AD; TPC-1) and unknown (H1568). **B)** Box plot of ratios between GI₅₀ values of cell lines with respective primary genotypic targets and non-target cell lines screened against the panel of inhibitors. **C)** Volcano plot depicting log₂-change of phosphorylation change plotted against the $-\log_{10}$ p-values from phosphoproteomic analyses. Among all detected phospho-peptides, receptor tyrosine kinases are highlighted in red.

Supplementary Figure 3

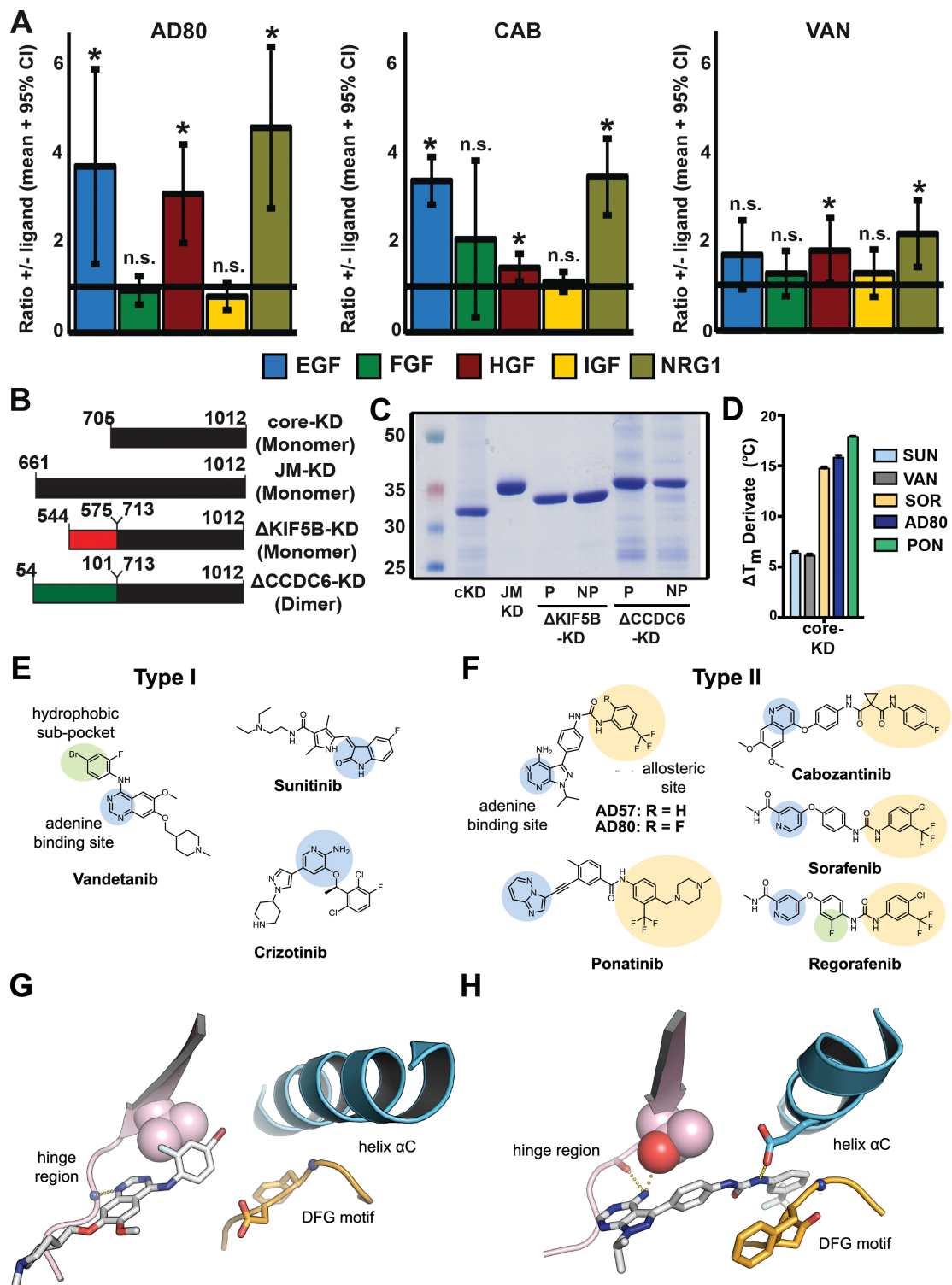


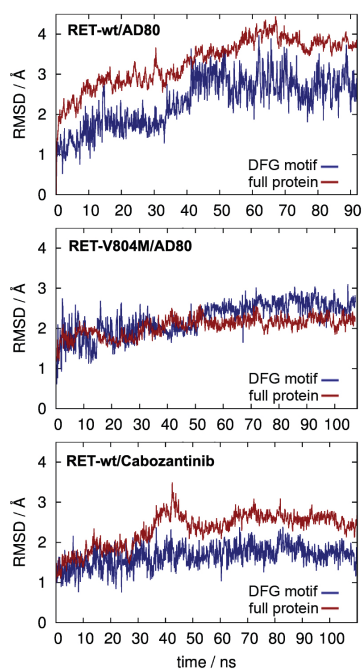
Fig. S3. Delineation of the cellular targets of AD80 using ligand screens and thermal shift experiments and comparison of type I and II RET kinase inhibitors.

A) Effects of growth factor supplementation on the viability of LC-2/AD cells treated with indicated compounds. Bars indicate average across concentrations and experiments, errorbars show 95% confidence intervals of the mean (from n=4) B) Schematic presentation of the constructs used in the thermal stability assay:

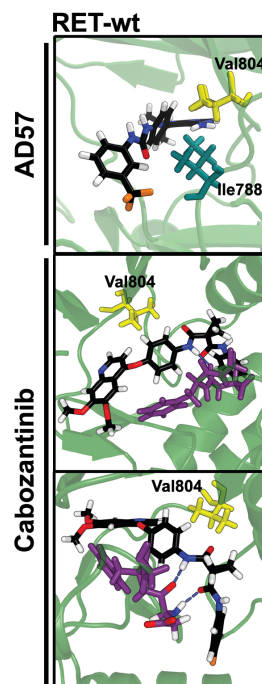
kinase domain (cKD), juxtamembrane-kinase domain (JM-KD), truncated Δ KIF5B-KD and Δ CCDC6-KD fusions proteins. **C)** Coomassie stained SDS-PAGE gel of purified proteins: core kinase domain (cKD) 705-1012, juxtamembrane-kinase domain (JM-KD) 661-1012, Truncated Δ KIF5B-KD and Δ CCDC6-KD fusions proteins in a non-phosphorylated (NP) or phosphorylated (P) state. Molecular weight markers (kDa) are shown as indicated. **D)** Differences in melting temperatures from AD80, sorafenib (SOR), vandetanib (VAN), ponatinib (PON) or sunitinib (SUN) addition (ΔT_m) and the respective standard errors of the mean (SEM) are shown for phosphorylated Core-KD. **E)** Overview of selected Type I kinase inhibitors and **F)** selected Type II kinase inhibitors with highlighted motifs addressing corresponding regions within the enzymes binding site. **G)** Vandetanib (Type I) in complex with RET kinase (PDB-entry: 2IVU) and **H)** AD57 (Type II) in complex with cSrc (PDB-entry 3EL8).

Supplementary Figure 4

A



B



C

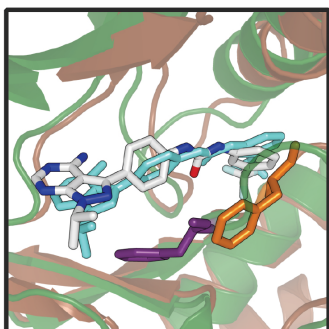


Fig. S4. Root mean square deviations (RMSD) measurements of RET and AD80 or cabozantinib and optimized structures after extensive MD refinement followed by ALPB optimization.

A) Root mean square deviations (RMSD) of RET-wt (top, bottom) and RET-V804M (middle) with AD80 (top, middle) and Cabozantinib (bottom) over simulation time, measured from the starting point of the respective simulations (middle and bottom data have been started essentially at the final top panel geometry). **B)** RET-wt/AD57 after 202 ns (92 ns from RET-wt/AD80 simulation followed by 110 ns TI-MD for gradually transforming AD80 into AD57, side view), (middle and lower panel) RET-wt/Cabozantinib after 112 ns from different perspectives, the latter allowing for H-bond identification. **C)** Superimposition of cSrc (brown, PDB code 3EL8) and RET-wt (green) in complex with AD57 (see also Fig. 3CII). The experimentally resolved ligand pose is shown in light blue with phenylalanine of the DFG motif in orange. The corresponding MD results are shown in element-specific colors for AD57 and in violet for Phe of DFG. The DFG motif is shown in violet. Images have been created with PyMOL (The PyMOL Molecular Graphics System, Version 1.8 Schrödinger,

LLC).

Supplementary Figure 5

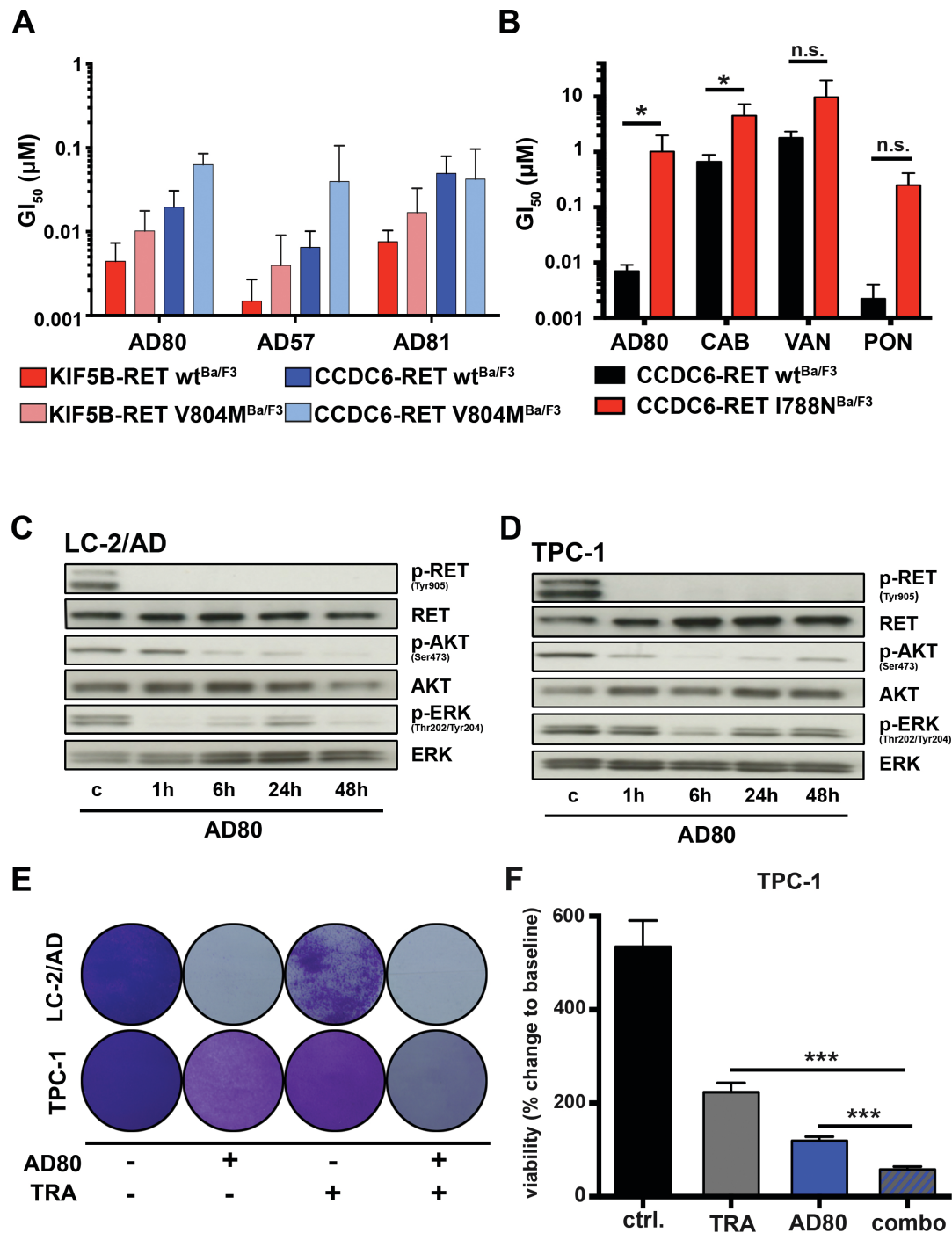


Fig. S5. Inhibitory potential of AD80 derivatives and primary and secondary resistance against RET inhibition.

A) Column chart of mean GI_{50} -values + SD (from $n \geq 3$) of Ba/F3 cells expressing wild type and V804M mutated *KIF5B-RET* or *CCDC6-RET* after 72h of treatment with AD80 and AD80 derivatives AD57 and AD81. **B)** Column chart of mean GI_{50} -values + SD (from $n \geq 3$) of Ba/F3 cells expressing *CCDC6-RET*^{wt} or *CCDC6-RET*^{V804M} after 72h of treatment as assessed for AD80, cabozantinib (CAB), vandetanib (VAN) and

ponatinib (PON) is shown. **C)** Immunoblot of LC-2/AD cells under treatment with AD80 (0.1 μ M) for 1h, 6h, 24h and 48h. **D)** The same experimental setting was also applied to TPC-1 cells. **E)** Clonogenic assay of TPC-1 and LC-2/AD cells under treatment (7d) with either AD80 (0.5 μ M), trametinib (0.5 μ M) or a combination of both inhibitors. Cells are visualized via crystal violet staining. **F)** TPC-1 cells were treated (72h) with AD80 (0.5 μ M) trametinib (TRA) (0.5 μ M) or with a combination of both. Cellular viability was assessed and is given as mean % change from baseline.

Supplementary Figure 6

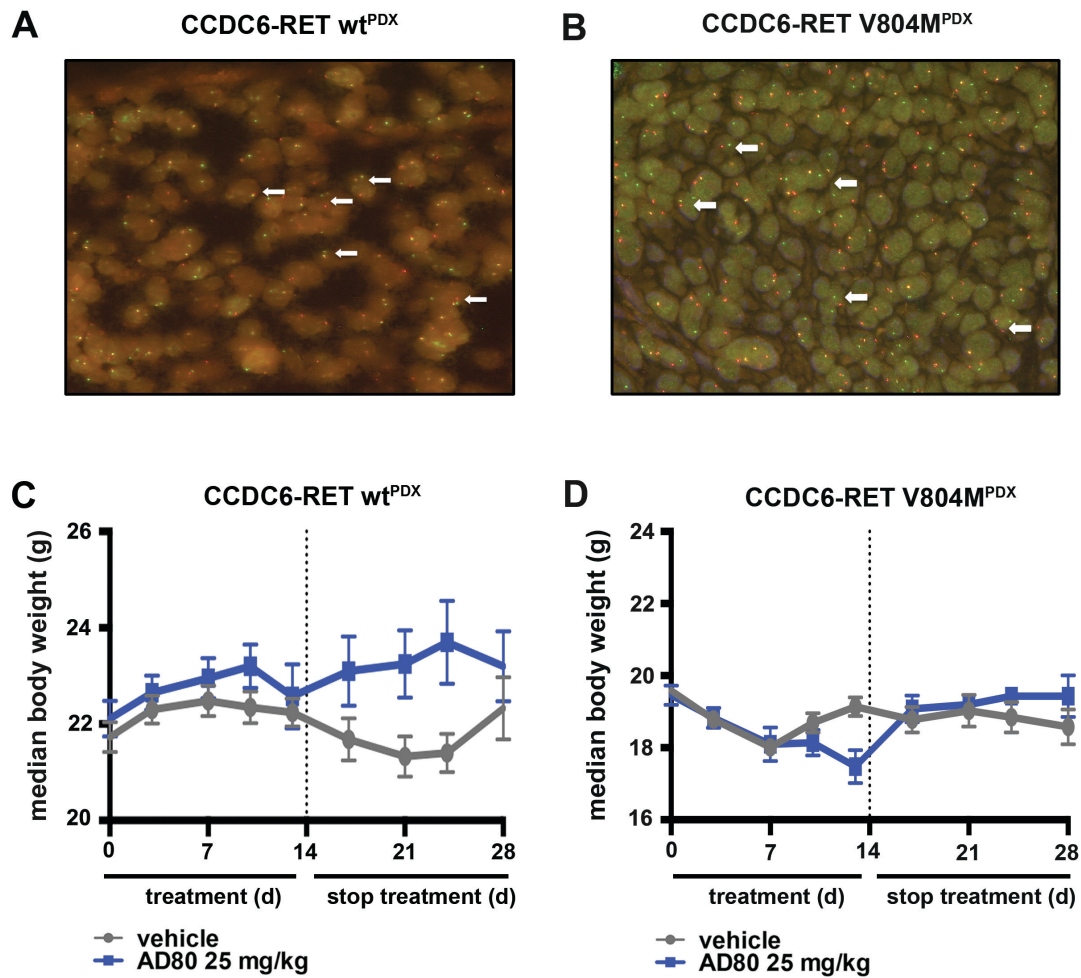


Fig. S6. Validation of PDX via FISH and *in vivo* effects induced by treatment with AD80.

A) An exemplary positive fluorescence in situ (FISH) break-apart analysis from mice engrafted with *CCDC6-RET* fusion positive patient-derived tumor tissue (*CCDC6-RET^{PDX}*) with split red and green signals is shown indicating *RET* gene rearrangements (white arrows). **B)** An equivalent FISH analysis from *CCDC6-RET V804M^{PDX}* is shown. **C)** Median body weight change of *CCDC6-RET^{PDX}* under treatment with AD80 (25 mg/kg) or vehicle control and 14 days of follow-up. **D)** The equivalent median body weight change for *CCDC6-RET V804M^{PDX}* is shown.

Supplementary Figure 7

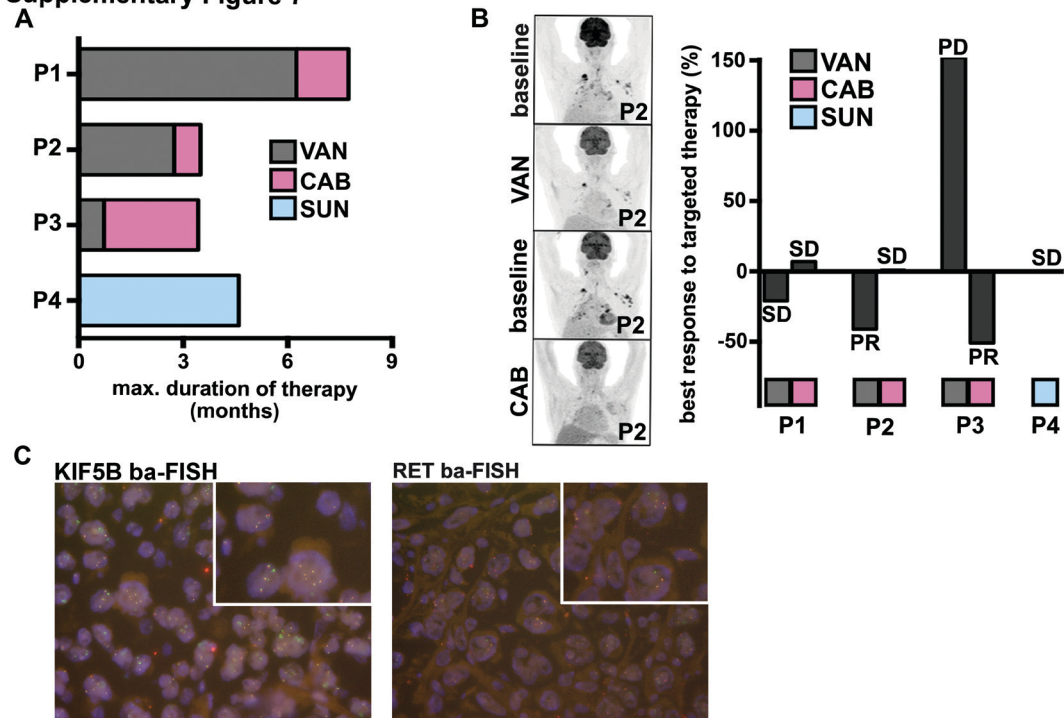


Fig. S7. Limited clinical activity of currently available RET inhibitors and validation of a small cohort of patients with *RET*-rearrangements.

A) Time of treatment for patients (P1-P4) that underwent therapy with either vandetanib (black), cabozantinib (rose) or sunitinib (light blue). **B)** Exemplary PET-CT scans of Patient P2 (P2) showing best response of target lesions (left panel). Waterfall plots for best response of target lesions measured with PET/CT scans to vandetanib (black), cabozantinib (rose) or sunitinib (light blue) for each patient (right panel). *PD*: progressive disease; *SD*: stable disease; *PR*: partial response. **C)** Representative break-apart FISH (ba-FISH) images of *KIF5B* and *RET* probes for diagnostics of *RET*-rearrangements in patient P3.

Supplemental Tables

Table S1. IC₅₀ values of AD80, cabozantinib and vandetanib for phospho-RET levels in Ba/F3 cells expressing wild type or V804M *KIF5B-RET*.

Overview of IC₅₀ values of phospho-RET signal from displayed immunoblots of Ba/F3 cells expressing wild type or V804M *KIF5B-RET* treated with AD80, cabozantinib and vandetanib.

Supplementary Table 1

Fitted IC₅₀ values (nM) quantified from immunoblot

| | AD80 | cabozantinib | vandetanib |
|-----------------|------|--------------|------------|
| KIF5B-RET-wt | 9.24 | 10.12 | NA |
| KIF5B-RET-V804M | 9.98 | NA | NA |

Table S2. GI₅₀ values of the panel of patient-derived cell lines.

A tabular overview of mean GI₅₀ values (from n=3) from various patient-derived cancer cell lines treated (72h) with AD80, alectinib (ALE), BGJ398 (BGJ), cabozantinib (CAB), ceritinib (CER), erlotinib (ERL), ponatinib (PON), regorafenib (REG) or vandetanib (VAN) is shown. GI₅₀ values are given in μM .

Supplementary Table 2Mean GI₅₀ (μM) values from n=3

| Cell Line | AD80 | Alectinib | BGJ398 | Cabozantinib | Ceritinib | Erlotinib | Ponatinib | Regorafenib | Vandetanib |
|-----------|-------|-----------|--------|--------------|-----------|-----------|-----------|-------------|------------|
| SKBR3 | 2.800 | >10 | >10 | >10 | >10 | 3.300 | 3.881 | 4.900 | 9.600 |
| H1781 | 1.800 | >10 | >10 | >10 | 7.200 | 5.300 | 3.559 | 9.834 | 9.900 |
| H1819 | 3.200 | >10 | >10 | >10 | 5.600 | 2.000 | 4.151 | 5.834 | 8.500 |
| H2228 | 0.280 | 3.300 | 7.400 | 3.906 | 1.700 | 9.700 | 3.797 | 6.400 | >10 |
| H520 | 2.800 | >10 | >10 | 8.888 | 8.500 | >10 | 0.835 | 3.967 | 4.500 |
| H1975 | 1.700 | >10 | >10 | >10 | 5.900 | 6.100 | 3.357 | 5.891 | >10 |
| PC9-GR | 0.710 | 7.400 | >10 | 7.268 | 2.900 | 0.720 | 5.702 | 6.884 | 1.600 |
| H441 | 1.400 | >10 | >10 | 9.156 | 4.600 | 5.300 | 3.458 | 7.749 | 4.300 |
| A549 | 3.267 | >10 | >10 | 5.366 | 3.436 | >10 | 4.968 | 5.622 | >10 |
| H1568 | 0.900 | 2.800 | >10 | 4.740 | 3.400 | 1.500 | 2.294 | 1.141 | 2.100 |
| LC-2/AD | 0.004 | 0.215 | >10 | 0.303 | 1.811 | 4.468 | 0.010 | 0.723 | 0.372 |
| TPC-1 | 0.340 | 0.664 | >10 | 1.992 | 5.990 | 9.502 | 0.333 | 2.375 | 3.901 |
| H3122 | 1.777 | 0.030 | >10 | 6.725 | 0.018 | >10 | 5.287 | 5.136 | >10 |
| H1581 | 0.210 | 5.225 | 0.032 | 0.721 | 1.766 | >10 | 0.574 | 0.369 | 5.275 |
| H1792 | 8.134 | >10 | >10 | 6.689 | 4.075 | >10 | 1.008 | 5.713 | >10 |
| HCC827 | 0.679 | 7.858 | >10 | 4.474 | 3.877 | 0.026 | 2.118 | 7.011 | 0.241 |
| PC9 | 6.582 | >10 | >10 | 5.946 | 3.133 | 0.038 | 5.151 | 8.907 | 1.366 |
| HCC44 | 0.415 | >10 | >10 | 3.674 | 3.913 | >10 | 1.455 | 3.215 | >10 |

Table S3. Tabulated derivative melting temperatures (T_m) and differences in melting temperature (ΔT_m) values.

Derivative melting temperatures (T_m) and differences in melting temperatures (ΔT_m) values and the respective SEM variance are shown. Proteins were incubated with 1 mM drug or equivalent volume of DMSO prior to experiment. Non-phosphorylated forms of each RET protein were extensively CIP-phosphatase treated to remove phospho-tyrosine. To activate the proteins, they were incubated either with Mg-ATP or with Mg-ATP and an active RET kinase protein to drive autophosphorylation. Thermal shift experiments were performed using between two and five independent preparations of each protein and were carried out in triplicates.

Supplementary Table 3

| Protein | Drug | T _m derivative | | ΔT _m Derivative | |
|------------|------------|---------------------------|----------------|----------------------------|----------------|
| | | Non-phosphorylated | Phosphorylated | Non-phosphorylated | Phosphorylated |
| ACCDC6-RET | No drug | 48.09 ± 0.19 | 47.81 ± 0.08 | 0.00 ± 0.00 | 0.00 ± 0.08 |
| | Sunitinib | 52.73 ± 0.96 | 52.33 ± 0.14 | 4.64 ± 0.77 | 4.52 ± 0.14 |
| | Vandetanib | 52.86 ± 0.65 | 52.61 ± 0.05 | 4.76 ± 0.45 | 4.80 ± 0.05 |
| | Sorafenib | 58.19 ± 0.76 | 58.50 ± 0.17 | 10.10 ± 0.56 | 10.69 ± 0.17 |
| | AD80 | 59.02 ± 1.48 | 62.73 ± 0.06 | 10.93 ± 1.29 | 14.92 ± 0.06 |
| AKIF5B-RET | No drug | 45.40 ± 1.24 | 45.08 ± 0.72 | 0.00 ± 0.00 | 0.00 ± 0.00 |
| | Sunitinib | 46.99 ± 2.27 | 47.52 ± 1.81 | 1.59 ± 1.02 | 2.44 ± 1.45 |
| | Vandetanib | 49.28 ± 1.77 | 49.67 ± 2.03 | 3.88 ± 0.53 | 4.59 ± 1.64 |
| | Sorafenib | 58.31 ± 0.11 | 58.69 ± 0.16 | 12.91 ± 1.35 | 13.61 ± 1.05 |
| | AD80 | 61.79 ± 0.56 | 62.58 ± 0.24 | 16.39 ± 0.68 | 17.50 ± 0.68 |
| JM-KD | No drug | 41.78 ± 1.38 | 41.89 ± 0.54 | 0.00 ± 0.00 | 0.00 ± 0.00 |
| | Sunitinib | 44.08 ± 2.07 | 42.55 ± 0.38 | 0.93 ± 0.01 | 0.70 ± 0.80 |
| | Vandetanib | 44.22 ± 1.96 | 44.93 ± 0.50 | 1.48 ± 0.40 | 3.08 ± 0.68 |
| | Sorafenib | 54.44 ± 1.43 | 56.33 ± 0.61 | 12.66 ± 0.07 | 14.66 ± 0.23 |
| | AD80 | 54.36 ± 1.56 | 56.83 ± 0.76 | 12.58 ± 0.26 | 14.94 ± 0.71 |
| Core KD | No drug | 42.78 ± 0.27 | 43.01 ± 0.06 | 0.00 ± 0.27 | 0.00 ± 0.06 |
| | Sunitinib | 46.25 ± 0.19 | 49.34 ± 0.21 | 3.47 ± 0.19 | 6.33 ± 0.21 |
| | Vandetanib | 45.39 ± 0.11 | 49.11 ± 0.19 | 2.61 ± 0.11 | 6.11 ± 0.19 |
| | Sorafenib | 56.18 ± 0.15 | 57.74 ± 0.18 | 13.39 ± 0.15 | 14.73 ± 0.18 |
| | AD80 | 55.35 ± 0.20 | 58.82 ± 0.24 | 12.57 ± 0.20 | 15.81 ± 0.24 |

| Core KD | - | ATP | AD80 | cabozantinib | ponatinib | sorafenib |
|---------|-------|-------|-------|--------------|-----------|-----------|
| Ave TM | 42.28 | 46.96 | 55.22 | 57.01 | 61.24 | 55.85 |
| st dev | 0.29 | 0.00 | 0.72 | 0.29 | 0.18 | 0.18 |
| st err | 0.15 | 0.00 | 0.41 | 0.15 | 0.09 | 0.09 |
| Ave dTM | 0.00 | 4.67 | 12.69 | 13.92 | 17.87 | 13.20 |
| st dev | 0.29 | 0.00 | 0.75 | 0.34 | 0.18 | 0.18 |
| st err | 0.15 | 0.00 | 0.43 | 0.17 | 0.09 | 0.09 |

Table S4. *In vitro* kinase assay of RET wt, V804M and V804L mutants with different inhibitors.

An overview of IC₅₀ values of a panel of type I and II RET inhibitors determined via homogeneous time-resolved fluorescence (HTRF) *in vitro* kinase assay.

Supplementary Table 4

| type of binding | compound | RET wt | RET V804M | RET V804L |
|-----------------|--------------|--------------|-------------|--------------|
| | | IC 50 [nM] | IC 50 [nM] | IC 50 [nM] |
| type II | AD80 | 1.3 ± 0.2 | 0.4 ± 0.2 | 0.6 ± 0.3 |
| type II | ponatinib | 3.4 ± 0.2 | 4.7 ± 0.1 | 4.2 ± 0.3 |
| type I | crizotinib | 12.5 ± 0.9 | 90.9 ± 17.2 | 108.4 ± 18.4 |
| type II | cabozantinib | 23.7 ± 7.9 | 209.5 ± 8.6 | 150.0 ± 22.9 |
| type I | sunitinib | 30.5 ± 11.9 | 74.9 ± 19.7 | 69.0 ± 13.1 |
| type II | sorafenib | 63.7 ± 26.8 | 21.5 ± 6.5 | 32 ± 3 |
| type I | vandetanib | 382.3 ± 23.9 | >2000 | >2000 |

Table S5. Experimental setup for saturated mutagenesis screening.

An overview of the experimental setting for our saturated mutagenesis screening using XL1-RED E. coli is given. The primary RET construct transformed in XL1-RED E. coli, the duration of accelerated mutagenesis in these cells, the AD80 concentration at which transduced Ba/F3 cells were selected and the deep sequencing results are shown.

Supplementary Table 5

| Primary RET Construct | Mutagenesis Duration (h) | AD80 Selection (nM) | cDNA Change | Protein Change |
|------------------------------|---------------------------------|----------------------------|--------------------|-----------------------|
| CCDC6-RET | 24 | 200 | - | - |
| KIF5B-RET | 48 | 200 | - | - |
| CCDC6-RET | 72 | 200 | 2363 T>A | I788N |

Table S6. Clinical response rates to currently available anti-RET drugs and clinical information of patients used in retrospective analysis.

A) Publically available clinical data for progression-free survival (PFS) and objective response rates (ORR) from patients with *RET*-rearranged tumors treated either with cabozantinib (NCT01639508; Drilon *et al.*) or vandetanib (Gautschi *et al.* and Yoh *et al.*) are displayed. **B)** Best response rates to targeted therapy for each patient receiving vandetanib, cabozantinib or sunitinib therapy relative to baseline are displayed. Response was annotated as “progressive response” (PR), “steady disease” (SD) or “progressive disease” (PD) according to RECIST 1.1 criteria. The dosing of the individual drugs per patient is displayed. **C)** Overview of patients for *RET*-rearrangement and detection method.

Supplementary Table 6

A

| | Median ORR (%) | Median PFS (months) | cohort size |
|-------------------------------|----------------|---------------------|-------------|
| Drilon <i>et al.</i> | 28 | 7 | 20 |
| Gautschi <i>et al.</i> | nn | 6.25* | 1 |
| Yoh <i>et al.</i> | 53 | 4.7 | 17 |

* corresponds to patient P1

B

| | Vandetanib | Cabozantinib | Sunitinib |
|---------------|------------|--------------|---|
| dosage | 300 mg/d | 140 mg/d | 50 mg/d (4 weeks on – 2 weeks off); since cycle III dose reduction to 37.5 mg/d |
| P1 | - 21% (SD) | 7% (SD) | - |
| P2 | - 41% (PR) | 1% (SD) | - |
| P3 | 152% (PD) | - 51% (PR) | - |
| P4 | - | - | 0% (SD) |

C

| Patient | ba-FISH RET | ba-FISH KIF5B | hybrid capture-based next generation sequencing |
|---------|-------------|---------------|---|
| P1 | positive | positive | confirmation of KIF5B-RET rearrangement |
| P2 | positive | negative | |
| P3 | positive | positive | |
| P4 | positive | positive | |